

The Role of Turbulent Convection in the Primitive Solar Nebula

II. Results

W. CABOT, V. M. CANUTO, AND O. HUBICKYJ

*NASA Goddard Space Flight Center, Institute for Space Studies, 2880 Broadway,
New York, New York 10025*

AND

J. B. POLLACK

Space Science Division NASA-Ames Research Center, Moffett Field, California 94035

Received May 14, 1986; revised October 15, 1986

Numerical results from a new model of the primordial solar nebula are presented in which convection is assumed to be the sole source of turbulence that causes the nebula to evolve. We introduce a new model of convective turbulence (described in detail in Paper I of this series) and new grain opacities computed from an improved physical model. The nebula is assumed to be in a stage prior to planetesimal formation in which gas and dust grains are mixed homogeneously, but in a stage after significant infall of matter from the outer cloud. Vertical structures for a thin nebular disk are calculated for different radii and accretion rates assuming vertical hydrostatic and thermal equilibrium; radial sequences of vertical solutions are constructed for constant accretion rates to represent quasistatic disk structures. Some aspects of our results differ markedly from those done previously by Lin and co-workers. Our values for the turbulent efficiency α (10^{-2} to 10^{-4}) are much lower and much more sensitive to opacity and surface density. Our low values of α result in (1) small turbulent speeds ($\leq 1\%$ of sound speed), which will alter prior computations of grain coagulation and sedimentation rates; (2) a more massive disk ($>0.1M_{\odot}$) that becomes gravitationally unstable at outer (super-Uranian) orbits; (3) a lower "best value" of the accretion rate ($\sim 10^{18.5}$ g sec^{-1}); and (4) a longer characteristic dispersal time for the disk ($>2 \times 10^6$ years), which may greatly exceed that inferred from young stellar objects. The high sensitivity of α on surface density produces an inverse accretion rate-surface density relationship, which implies that the Lightman-Eardley diffusive instability develops throughout a steady disk structure in the radial direction, causing the disk, at least at the onset, to separate into rings. Because radial gradients are neglected in the base disk structure, the manner in which the instability evolves to finite amplitude is unknown, but it could prevent the disk from reaching a quasistatic structure altogether. We conclude that convection may not be the dominant source of turbulence needed to evolve young solar/stellar nebulae, and may in fact be a disruptive mechanism in disk structure. © 1987 Academic Press, Inc.

I. INTRODUCTION

The inner disklike region of the primordial solar nebula has been modeled and studied with respect to protoplanetary formation by Lin and co-workers (Lin and Papanoizou, 1980; Lin, 1981; Lin and Bodenheimer, 1982; referred to hereafter as LPB) using simplifying assumptions from thin accretion disk theory (cf. Pringle, 1981) and assuming that the disk is viscously cou-

pled by turbulence driven solely by thermal convection. LPB used a modified form of stellar mixing length theory (MLT) to estimate convective heat transport, mean speeds of convective motions, and turbulent (Reynolds) stresses. The nebular material was assumed to be a homogeneous mixture of gas and dust grains, with the latter providing virtually all of the material's opacity. LPB used grain opacity relations published by DeCampli and Cameron

(1979). LPB were able with their method to construct quasistatic (constant accretion rate) models of thin disks (loosely constrained by the distribution of present planetary debris) which are stable against radial disturbances.

Cabot *et al.* (1987; hereafter Paper I) re-examine this problem in light of a new model for large-scale turbulence proposed by Canuto *et al.* (1984) and Canuto and Goldman (1985; hereafter CG), which allows them to include the effects of rotation on convective motions. In Paper I the theoretical development of the thin-disk structure equations for the solar nebula with CG's method is presented and compared extensively with that of LPB. In this paper we present the numerical results from that work, also using the new grain opacities by Pollack *et al.* (1986). We compare these results with those of LPB and with still uncertain observational constraints. In particular, we speculate on the apparently unstable nature of our new models. In Section II the vertical structure equations for the numerical analysis are presented. In Section III we discuss the new Pollack grain opacities. In Section IV the numerical results are presented and analyzed with respect to constraints similar to those imposed by LPB. In Section V we analyze the stability of our numerical models, especially with regard to the radial viscous (Lightman-Eardley) instability and gravitational (Jean's) instability. In Section VI we investigate possible consequences of the gravitational instability on the disk structure. Finally, the implications of our models toward the archetypical LPB models and toward the nature of young stellar systems are examined in Sections VII and VIII.

II. THE LOCAL VERTICAL STRUCTURE OF THE DISK

(a) *The Local Vertical Structure Equations of a Thin Disk*

We employ the standard vertical structure equation for a stationary, quasi-Keplerian thin disk in which self-gravity is negli-

gible (Pringle, 1981). The thin-disk approximation is valid when

$$z/R \ll 1, \quad (1)$$

for all heights above midplane ($z = 0$) at cylindrical radius R . The self-gravity of the disk material is considered negligible when the vertical gravitational force due to the central object GMz/R^3 is much greater than that due to the disk material (roughly $2\pi G\rho z$), i.e.,

$$\frac{GM}{R^3} \gg 2\pi G\rho, \quad (2)$$

where M is the mass of the central object, and ρ is the density of the disk material. We test conditions (1) and (2) a posteriori. We limit our considerations to models that are optically thick (with the provisions discussed in Sect. IVc), since we do not expect an optically thin disk to be capable of sustaining a superadiabatic temperature gradient.

In the thin-disk approximation, the vertical structure at a selected radius is computed neglecting radial derivatives of thermodynamic variables. All thermodynamic quantities that appear in the vertical structure equations in this section represent mean ambient values in the presence of convection.

The vertical hydrostatic equilibrium condition is given by

$$\frac{dp}{dz} = -\rho g, \quad (3)$$

where p is the total pressure and g is the local effective gravity

$$g = \Omega^2 z, \quad (4)$$

with the rotation rate Ω given by

$$\Omega^2 = \frac{GM}{R^3}. \quad (5)$$

The presence of turbulence will modify the vertical structure (Eq. (3)) through the presence of a turbulent pressure, $p_t = \rho v_t^2$, where v_t is the turbulent velocity; p_t should be added to the gas pressure p on the left-

hand side of Eq. (3). Using the model of turbulence as described in Section IV in Paper I, we have computed the value of v_t^2 and found a posteriori that ρ_t is less than 0.1% of the gas pressure p in all relevant cases. We have therefore neglected the turbulent component of the pressure in order to simplify the computation, although it can in principle be included (see Sect. IV in Paper I).

The energy equation is given by Eqs. (1) and (2) (Sect. II in Paper I):

$$\frac{dF}{dz} = \rho \langle \nu_t \rangle \left(R \frac{d\Omega}{dR} \right)^2 = \frac{9}{4} \rho \langle \nu_t \rangle \Omega^2, \quad (6)$$

where $\langle \nu_t \rangle$ is the constant density-averaged coefficient of turbulent viscosity. The total flux,

$$F = F_r + F_c, \quad (7)$$

is composed of the radiative flux F_r , which is given in optically thick media by the radiative diffusion equation,

$$F_r = - \frac{4acT^3}{3\rho\kappa} \frac{dT}{dz} = -c_p \rho \chi \frac{dT}{dz}, \quad (8)$$

and of the convective flux F_c , evaluated in Section III in Paper I. In Eq. (8), T is the temperature, κ the Rosseland mean opacity, c_p the specific heat at constant pressure, χ the coefficient of radiative conductivity, a the radiation constant, and c the speed of light.

(b) Equation of State and Specific Heat

The equation of state is assumed to be a perfect gas with radiation pressure (see Cox and Giuli, 1968; Clayton, 1968). The total pressure (neglecting turbulent pressure) is given by

$$p = \bar{R}_g \rho T + \frac{1}{3} a T^4 \equiv \bar{R}_g \rho T / \beta_g, \quad (9)$$

where β_g is the ratio of gas pressure ($\bar{R}_g \rho T$) to total pressure (p). The effective gas constant \bar{R}_g is given by $\bar{R}_g = N_A k / \bar{\mu}$, where N_A is Avogadro's number, k is Boltzmann's constant, and $\bar{\mu}$ is the mean molecular weight.

The nondimensional adiabatic temperature gradient (∇_{ad}) is given in terms of the specific heat at constant pressure by

$$\nabla_{\text{ad}} = (1/\beta_g)(4/\beta_g - 3)\bar{R}_g/c_p. \quad (10)$$

We assume that the nebula has the solar composition ($X = 0.73$, $Y = 0.25$) given by Allen (1973). In order to compute $\bar{\mu}$ and c_p , we further assume that all of the hydrogen is molecular (H_2) and in its electronic ground state, and that the helium and metals are atomic and electronically neutral. At the low temperatures encountered in our models, H_2 does not dissociate appreciably, and so we take $\bar{\mu}$ as a constant equaling 2.34.

The specific heat of H_2 has a strong temperature dependence for $T < 300^\circ\text{K}$ due to rotational-vibrational transitions. There may also be departures from thermal equilibrium between *ortho* and *para* modifications (cf. Herzberg, 1950; Osterbrock, 1962; DeCampi *et al.*, 1978). The conversion rate between *ortho* (parallel nuclear spins) and *para* (antiparallel nuclear spins) modifications is forbidden, and therefore very slow, unless catalysts (such as grains) are present in sufficient quantity to speed the conversion. The relative population of the modifications in the solar nebula depends on the rather uncertain thermal history of the material and the amount of catalysis that occurred.

We concern ourselves with three possible mixtures of *para* and *ortho* modifications in H_2 . At STP the normal mixture is 3:1 *ortho* to *para*, corresponding to thermal equilibrium between modifications. The 3:1 ratio of *ortho* to *para* for general thermodynamic conditions is known as the "statistical mixture." An H_2 gas may be frozen in the statistical mixture at low temperatures and densities by the very slow conversion rates, even though the *ortho* and *para* modifications are not in thermal equilibrium. Given sufficient time the *ortho* modification will become almost completely depopulated at low temperatures, resulting in almost pure *para* H_2 ; upon re-

heating, the *para* modification may remain dominant for slow conversion rates. If catalysis occurs in an amount sufficient to produce almost free conversion between modifications, thermal equilibrium would occur between modifications at all temperatures and densities, giving an "equilibrium mixture." Because we are uncertain about the conversion rates between modifications in the solar nebula, we compute models with specific heats corresponding to all three mixtures (statistical mixture, equilibrium mixture, and pure *para* modification) at low temperatures where they differ greatly.

The temperature range where rotational-vibrational transitions and the *para-ortho* modifications are important is coincidentally where the opacities from water-ice grains are important. For low-temperature models with midplane convection driven by water-ice opacities, we compute c_p for H_2 in its electronic ground state from the molecular constants given in Herzberg (1950) and Allen (1973) for the three *para-ortho* mixtures of interest. In the statistical mixture c_p rises smoothly from 2.5 (in units of \bar{R}_g) at $T \leq 50^\circ K$ to about 3.1 at $T = 150^\circ K$ and levels off to 3.5 at $T = 300^\circ K$. In the equilibrium mixture c_p rises rapidly from 2.5 at $T \leq 15^\circ K$ to a peak value of about 4.8 near $50^\circ K$, drops rapidly to about 3.2 at $140^\circ K$, and rises slowly toward 3.5, asymptotically merging with values of the statistical mixture. In the *para* modification c_p rises rapidly from 2.5 for $T \leq 40^\circ K$ to a peak of 4.0 at about $170^\circ K$ and falls to 3.6 at $300^\circ K$. All mixtures give virtually the same specific heat for $T \geq 300^\circ K$. For $T > 700^\circ K$, c_p rises slowly from about 3.5 to 3.8 at $T = 1400^\circ K$ (cf. Fig. 1 in DeCampli *et al.*, 1978). In all models, we assume for simplicity that the helium and metals have 3 degrees of thermodynamic freedom such that their specific heats are a constant 2.5. In reality, phase transitions of the grain material will cause variations in the specific heats of the metals. However, we suspect that this variation will be small in the aggregate c_p since

the grains/metals represent only about 2% of the solar composition by mass.

The radiation pressure is much smaller than the gas pressure in all models computed, so that $\beta_g \approx 1$ in Eq. (10). At very low temperatures $c_p \approx 2.5\bar{R}_g$ and $\nabla_{ad} \approx 0.40$. For high temperatures, with $c_p(H_2) = 3.5\bar{R}_g$, the solar composition gives $c_p = 3.35\bar{R}_g$ and $\nabla_{ad} \approx 0.30$.

(c) Optical Surface Boundary Conditions

The numerical integrator begins at height $z = H$ and a temperature equal to the effective temperature T_e defined in terms of the surface flux $F(H)$,

$$\frac{ac}{4} T_e^4 \equiv F(H), \quad (11)$$

at an optical depth τ of $\frac{2}{3}$. The density and pressure near the optical surface decrease with increasing z roughly as

$$\exp(-z^2/2h^2), \quad (12)$$

where h is the isothermal pressure scale height,

$$h^2 = \bar{R}_g T / \Omega^2. \quad (13)$$

Therefore the atmosphere is assumed to be confined for the most part to a narrow spatial region in which the gravity g can be assumed to be almost constant. The gray atmosphere boundary condition is given from hydrostatic equilibrium by

$$p(\tau) = g \int_0^\tau \kappa^{-1} d\tau \quad (14)$$

evaluated at $\tau = \frac{2}{3}$. The integration over the inverse opacity is accomplished by assuming a standard gray atmosphere temperature distribution:

$$T^4 = T_e^4 (3\tau/4 + \frac{1}{2}). \quad (15)$$

The opacity depends almost solely on temperature, depending only on density (or pressure) to the extent of determining condensation boundaries of the various types of grains (Sects. IV and V).

Integrating from $\tau = \frac{2}{3}$ precludes the computation of optically thin models ($\tau \lesssim 1$);

the use of the diffusion approximation for the flux (Eq. (8)) is inappropriate anyway for $\tau \lesssim 10$. More accurate atmosphere equations for thin slabs are required for the modeling of such optically thin disks.

(d) Midplane Boundary Conditions

At $z = 0$, one physically requires that the radiation and convection components of the flux vanish. Concomitant with this is the requirement that the temperature, density, and other thermodynamic quantities reach asymptotically constant values, i.e., their first derivative in z vanishes at $z = 0$. Furthermore, the energy generation rate, equivalently the turbulent viscosity, should be physically well behaved at midplane.

(e) Convective Fluxes and Viscosities Tables

The dimensionless function, $\Phi = \chi_t/\chi$, representing the convective flux and the function, ν_t/χ , representing the turbulent viscosity are read from Tables I and II in Paper I in $\log Ro$ and $\log S$ using a bicubic spline interpolation. This expedites the numerical computations in avoiding computation of the spectral function $E(k)$ and the sum of the growth rates $n(k)$ for each convective zone. At the edge of the convective regions and near midplane, the convective buoyancy is small enough that values of Ro and S are encountered that are off the tables, typically when $\Phi < 10^{-7}$. In this case, the flux is taken as zero and the values of ν_t/χ are estimated from an asymptotic analytical expression for the growth rates in relation (11) (Sect. III in Paper I).

Unlike the MLT, we have no explicit analytical expression to compute the true ambient temperature gradient consistently in the presence of a convective flux. Therefore, the radiative and convective components of the flux are iterated numerically to a consistent solution at each zone, for which the "radiative" temperature gradient from the total flux and the adiabatic temperature gradient from thermodynamic conditions are known.

(f) Grain Opacity Functions

The opacity (discussed in detail in Sect. III) has no density dependence in the range of densities and temperatures that we encounter in the solar nebula models, other than delineating condensation boundaries in temperature. In nature, the width in temperature of condensation boundaries is narrow but finite. However, the grid spacing of the opacity tables by Pollack *et al.* (1986) is too coarse to resolve the precise width and shape of the rapid declines in opacity at evaporation boundaries. In order to simplify the numerical procedure and avoid spurious results that can arise from two-dimensional interpolations, we assume that the transition in opacity across a condensation boundary is abrupt. The opacity is computed as several one-dimensional functions of temperature only fitted with a Lagrangian third-order polynomial interpolation; the appropriate function is determined by the species of grains present at the particular density and temperature, which is encoded separately.

Finite-step numerical integrations sometimes oscillate on the discontinuous condensation boundary, especially, we find, near the optical surface. When this problem is encountered, we introduce a finite transition region in the condensation boundary with a width of 1% of the grid spacing in temperature. This allows the numerical integration to proceed smoothly. We have also performed some numerical integrations with linear interpolations in the Pollack opacity grid across condensation boundaries, in which the opacity declines 100 times slower than in the previous scheme. We find no qualitative difference, other than allowing convection driven by opacity peaks to extend to temperatures a few degrees higher, since the decline in opacity is still quite steep.

(g) Numerical Procedure

The structure Eqs. (3), (6), and (8) were integrated with a fifth-order Runge-Kutta

predictor–corrector integrator. The independent variable is the vertical coordinate z . The stepsize in z is varied accordingly to the predicted accuracy of the solutions. This automatically aligns the vertical zones with rapidly varying or discontinuous physical features, such as opacity edges and radiative–convective boundaries.

The vertical integrations are performed for an annulus at a given radius R and effective temperature T_e . A trial height H_0 is chosen to be the height of the optical surface at an optical depth τ of $\frac{2}{3}$. The structure equations are integrated inward toward midplane, $z = 0$, with a trial value for the constant, averaged turbulent viscosity, ν_t^* , in the energy equation (6). The integration proceeds to $z = 10^{-5} H_0$, where physical quantities are linearly extrapolated to $z = 0$, in order to limit the number of vertical zones. If ν_t^* is too large, then the flux becomes negative for some positive value of z , at which point the integration is stopped and ν_t^* is decreased; if the chosen initial ν_t^* is too small, then the flux has a positive residual value at $z = 0$, and ν_t^* is increased. The value of ν_t^* consistent with H_0 is trapped and adjusted iteratively until the residual flux vanishes to sufficient accuracy. Once $\nu_t^*(H_0)$ satisfies $F(0) = 0$, ν_t^* is compared with the density-averaged value of $\langle \nu_t \rangle$ (see Sect. VI in Paper I) a posteriori from the local thermodynamic structure. If $\langle \nu_t \rangle < \nu_t^*$, then H_0 is decreased; if $\langle \nu_t \rangle \gg \nu_t^*$, then H_0 is increased and the ν_t^* satisfying $F(0) = 0$ is again sought. The values of H_0 are iterated until

$$\langle \nu_t \rangle = \nu_t^*. \quad (16)$$

The vertical scale, d , that appears in Eq. (6) (Sect. III in Paper I) is chosen as constant throughout a convective region and equal to the vertical size of the convective region. (This is in fact the very definition under which the local growth rates are derived from the linear analysis.) When convection reaches midplane, d is chosen as the total vertical extent of the convective region above and below midplane; in this case,

d is determined simply by height at which midplane convection sets in during the inward integration. When a convective layer does not extend to midplane, its extent is determined a posteriori and adjusted iteratively in subsequent integrations. The averaging process over the turbulent viscosity is not carried out for convective layers that do not extend to midplane; rather, the local value of ν_t is employed in the energy equation, since it is only the midplane solution that runs afoul mathematically with locally computed ν_t .

III. THE MODEL FOR THE GRAIN OPACITY

In order to evaluate radiative heating rates and radiative equilibrium temperature gradients, we have used the standard “diffusion” approximation to the equation of radiative transfer (Clayton, 1968). Within the context of this approximation, the key measure of the radiative opacity of the solar nebula is the Rosseland mean opacity, a wavelength weighted mean of the inverse of the monochromatic opacity and the temperature derivative of the monochromatic Planck function. Since at the temperatures of interest ($< 1500^\circ\text{K}$) small grains are the dominant source of opacity, we neglected the very small contribution due to gases. Values for the Rosseland mean opacity, κ , of the dust grains were obtained from the calculations of Pollack *et al.* (1986). Pioneering calculations of κ for a variety of grain species were made by Knacke (1968), Kellman and Gaustad (1969), and Cameron and Pine (1973). The new calculations of Pollack *et al.* (1986) represent a significant improvement over the earlier calculations by considering a more complete ensemble of grain species, by using better sets of optical constants, by using optical constants over a more complete range of wavelengths, and by averaging the opacity of various grain species on a monochromatic level.

Some recent models of the solar nebula (e.g., Lin and Papaloizou, 1980) have employed values of κ given by DeCampi and

Cameron (1979). At low temperatures ($\leq 200^\circ\text{K}$), these values were based on the early, unpublished results of Pollack *et al.* (1986), while at higher temperatures, they were derived in an independent, approximate fashion. The new results of Pollack *et al.* (1986) differ significantly from the latter values of DeCampli and Cameron both with respect to their absolute values and their dependence on temperature. In particular, κ is found by Pollack *et al.* (1986) to have only very weak dependence on temperature above the sublimation temperature for water ice, a result that has important implications for the extent of the thermal convective zone in the solar nebula. Pollack *et al.* (1986) also explored the dependence of κ on the particle size distribution for a very large range of sizes. Their procedure for determining κ is briefly summarized below.

Since grains scatter as well as absorb thermal radiation, one cannot use the traditional formula for the Rosseland mean opacity (e.g., Clayton, 1968). This formula is valid only for isotropic scattering or scattering involving phase functions that can be expanded in *even* functions of Legendre polynomials (e.g., Rayleigh scattering). However, grains having a size comparable to or greater than a wavelength have prominent asymmetrical phase functions. Pollack *et al.* (1986) derived a more general form for κ that allows for asymmetrical phase functions.

In order to evaluate κ , the composition of the dust grains, the optical constants of each of their components, and their size distribution need to be specified. The composition of the dust grains was derived chiefly from the thermodynamic equilibrium calculations of Lewis (1974) for a nebula having solar elemental abundance (Cameron, 1973). Lewis's results were used to specify the temperature stability boundaries of the key condensates as a function of the gas density of the nebula. Prime condensates included metallic iron, silicates, and water. The silicates were subdivided into a high-temperature form and a low-

temperature form (the latter have water of hydration), and these forms were further divided into components with and without iron. In addition to the above thermodynamic equilibrium components, a small amount of magnetite was included in the grain assembly since it is a common component of some meteorites and is suspected to be present in interstellar grains. The values of κ are not strongly influenced by the presence of magnetite.

For each component of the grain assembly, optical constants were derived from a host of laboratory measurements that covered the very broad spectral domain from the near ultraviolet to the microwave. Such a broad spectral coverage is needed in order to properly evaluate the wavelength integral equation for κ at the temperatures of interest.

Mie scattering theory was used to evaluate the monochromatic absorption and scattering coefficients for each component of the grain ensemble. These results were approximately combined and *then* integrated over wavelength. These calculations were made over a wide range of temperatures ($10\text{--}2500^\circ\text{K}$) and gas densities ($10^{-14}\text{--}1\text{ g cm}^{-3}$). Separate calculations were performed for a wide variety of particle size distributions. In each case, the same size distribution was used for all the components of the grain ensemble.

Figure 1 illustrates the temperature dependence of κ at a nebula density of 10^{-8} g cm^{-3} for a "nominal" size distribution (solid curve) and for ones in which the nominal distribution has been uniformly shifted in size by factors of 0.1 and 10. The nominal size distribution was derived from that characterizing interstellar dust grains (Mathis *et al.*, 1977). The number of grains of radius r varies as $r^{-3.5}$ for r between 0.005 and $1\ \mu\text{m}$, with a constant value for r of less than $0.005\ \mu\text{m}$ and a strong decrease with increasing r for r greater than $1\ \mu\text{m}$ (Pollack *et al.*, 1986, Eq. (6)).

The abrupt decreases in κ in Fig. 1 are due to the evaporation of grain species at

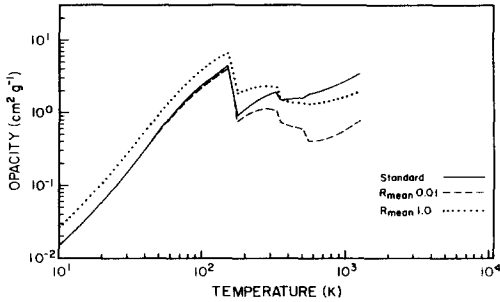


FIG. 1. The Rosseland mean extinction coefficients for a nominal size distribution as a function of temperature for a density of $10^{-8} \text{ g cm}^{-3}$. For comparison, curves with uniform scaling in particle radius, a factor of 10 larger and 100 times smaller, are included.

temperatures outside their stability fields. For example, the sharp decline of κ with increasing temperature near 175°K is due to the sublimation of water ice.

As illustrated in Fig. 1, κ does not depend sensitively on the exact choice of the size distribution function, which is fortunate since this function cannot be specified in any precise manner for the primordial solar nebula. The values of κ for the "nominal" size distributions were used in all the calculations of this paper. Thus, they are most pertinent to an early stage in the evolution of the primordial solar nebula, a stage in

which most grains had not yet accreted together to form much larger particles ($r > 30 \mu\text{m}$). When r becomes sufficiently large, κ has a much flatter dependence on wavenumber k and it becomes progressively smaller in magnitude with increasing r .

The temperature dependence of κ is one important factor in determining the extent of the convectively unstable regions of the nebula. In particular, if we assume $\kappa \sim T^\xi$, where T is temperature and ξ a constant, the radiative equilibrium temperature gradient is more likely to be convectively unstable when $\xi \gg 0$ (Lin, 1981). The function $\xi = \partial \ln \kappa / \partial \ln T$ for the opacities of Pollack *et al.* (1986) are shown in Fig. 2. According to Figs. 1 and 2, extensive altitude regions of thermal convection are most easily achieved at temperatures where water ice is present ($T < 175^\circ\text{K}$).

IV. RESULTS OF THE PRESENT WORK: NO SELF-GRAVITY

(a) Types of Solutions

We discuss initially the types of convective zones encountered in the numerical integrations and from which of these consistent solutions can be obtained. In order to obtain a consistent solution, the convection

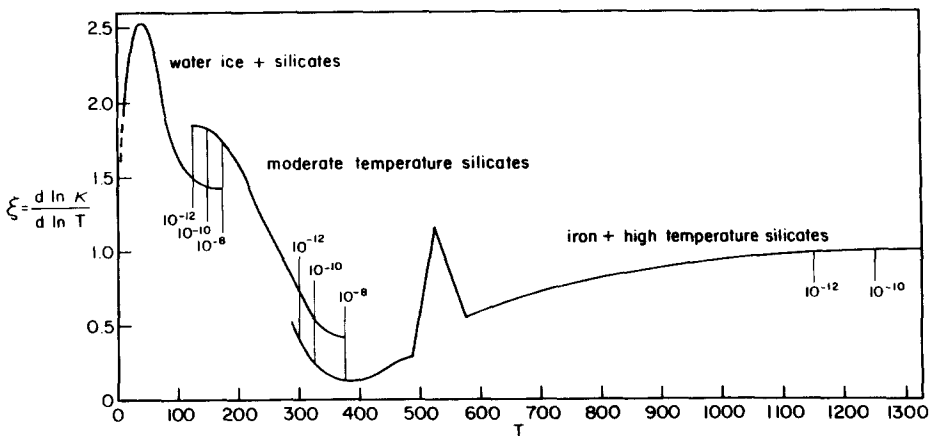


FIG. 2. The slope of opacity with temperature, $\xi = (d \ln \kappa) / (d \ln T)$, for the opacities of Fig. 1. The cutoff points of the opacity peaks for selected densities relevant to the solar nebula, 10^{-12} , 10^{-10} , and $10^{-8} \text{ g cm}^{-3}$, are indicated by labeling vertical lines. The spike at $T = 525^\circ\text{K}$ is due to a rapid increase in iron-grain opacities.

zone(s) must produce a sufficient amount of energy deposition via Eq. (6) (Sect. II) to balance the given amount of surface flux. This requires that the ambient temperature gradient be superadiabatic over a thick enough vertical extent. From the diffusion equation (8) (Sect. II), the dimensionless temperature gradient is

$$\nabla \equiv \frac{d \ln T}{d \ln p} = \frac{p F_r(z)}{g c_p \rho^2 \chi T} = \frac{3 \kappa p F_r(z)}{4 a c T^4 \Omega^2 z}. \quad (17)$$

Thus the vertical extent of the convection zone(s) is (are) mediated to a large degree by the run of opacities from $T = T_e$ at the optical surface to $T = T_c$ at midplane. The range of temperatures depends in turn on the opacities and thickness of the disk through the optical depth to midplane,

$$\tau_c = \int_0^\infty \kappa \rho dz = \frac{2}{3} + \int_0^H \kappa \rho dz, \quad (18)$$

since $T_c \sim \tau_c^{1/4} T_e$ in pure radiative equilibrium.

The presence of convection throughout a sizeable vertical extent depends not only on the size of the opacity but also on its shape as a function of temperature. Lin and Papaloizou (1980) have shown that opacities with large positive slopes in temperature facilitate the outbreak of convection. They showed that, for any form of the energy generation rate, $\nabla \geq 1/(4 - \xi)$, where $\kappa = \kappa_0 T^\xi$. Since $\nabla > \nabla_{\text{ad}}$ is required for convection, the condition $1/(4 - \xi) \geq \nabla_{\text{ad}}$ ensures the occurrence of convection. For $\nabla_{\text{ad}} = 0.30$ (appropriate for high temperatures), this condition gives $\xi \geq \frac{2}{3}$; and for $\nabla_{\text{ad}} = 0.40$ (appropriate for the lowest temperatures), it gives $\xi \geq \frac{1}{2}$. (Note that this is not a strict criterion for the presence of convection, since $1/(4 - \xi)$ is only a lower limit for ∇ .) The DeCampli–Cameron grain opacities have $\xi = 2$ for nearly all temperatures, and so are ensured of producing widespread convection.

The grain opacities by Pollack *et al.* (1986) have three peaks associated with the evaporation/condensation of different kinds of grains (see Fig. 1). We find that each

opacity peak is capable of sustaining superadiabatic temperature gradients and convection zones of varying thicknesses in the vertical structures. This result is also consistent with the aforementioned analysis by Lin and Papaloizou (1980). In Fig. 2, we show the power dependence of the opacity on temperature ($\xi = d \ln \kappa / d \ln T$) for the Pollack grain opacities. Except for the low-temperature end, with opacities due primarily to water-ice grains, the values of ξ tend to be well below 2. However, the values of ξ are large enough to satisfy Lin and Papaloizou's (1980) relation at least marginally, except for the depressed region around $T = 400^\circ\text{K}$. In practice we find that ∇ somewhat exceeds $1/(4 - \xi)$ and that convection can be driven at most temperatures with the Pollack opacities. For the higher temperature models, where $\xi \leq 1$, the convection for the Pollack opacities is much less efficient (and thus requires thicker disks) than that for the DeCampli–Cameron opacities.

We find that consistent models can be constructed only when a large midplane convective zone occurs. Consider an opacity that increases with increasing temperature, rises to a peak value at $T = T_\kappa$, and falls precipitously to a low value for T just greater than T_κ . The inward integration begins at the optical surface, $z = H$, with $T < T_\kappa$. Convection breaks out in the interior and, if H (i.e., τ_c) is not too large, $T_c < T_\kappa$, such that convection extends all the way to midplane. For such situations with midplane convection, increasing H causes the size of the convection zone, and thus the total energy deposition by turbulence, to increase. A consistent model with midplane convection is found if there exists a value of H such that $T_c \leq T_\kappa$ and the turbulent energy deposition balances the surface flux. However, if we increase the value of $T_c (< T_\kappa)$, we eventually find a point where the value of H corresponding to $T_c = T_\kappa$ is still too thin to account for all of the surface flux. Increasing H to the point that $T_c > T_\kappa$ causes the opacity and the temperature gra-

dient to plummet and the model to become radiative near midplane.¹ We are unable to force the convective layer to produce more energy by increasing H further. Increasing H causes the bottom boundary of the convective layer to rise away from midplane faster than the top boundary, such that the convective layer becomes thinner overall. Raising the convective layer closer to the optical surface causes the superadiabatic temperature gradient and the convective efficiency to decrease. These effects all cause the total amount of energy deposition in the convective layer to decrease when H is increased. We are therefore unable to find consistent models with one or more convective layers and a radiative midplane in our model. It is, however, possible to find consistent solutions with one or more convective layers provided that a substantial region of midplane convection can be driven by a rise in opacities at much higher temperatures.

We find it convenient to classify the types of consistent solutions by the primary source of opacity driving the midplane convection. The exact temperature of the opacity peaks (T_κ) depends on the density.

(1) “*Ice models*”: $T_c \leq T_\kappa^{ice} \approx 125$ to 175°K . Convection only occurs at midplane and is driven by the low-temperature opacity peak due primarily to water-ice grains.

(2) “*Silicate models*”: $T_c \leq T_\kappa^{si} \approx 325$ to 375°K . Midplane convection is driven by the opacity peak due primarily to moderate-temperature silicate grains. These solutions typically have a second, elevated convective layer due to water-ice opacities. In some models, though, the water-ice opacity peak lies so near the optical surface that no convective layer is formed.

¹ Because there is a residual flux remaining as one approaches $z = 0$, the temperature gradient must eventually become superadiabatic again, causing a very thin, “forced” convective region near $z = 0$. However, this thin, unphysical convective region typically provides a negligible amount of turbulent energy deposition, and so it can be safely ignored for the purpose of this discussion.

(3) “*Iron models*”: $T_c \leq T_\kappa^{Fe} \approx 1200$ to 1400°K . Midplane convection is driven by opacities from high-temperature silicate grains and iron grains. These solutions may feature no additional convective layers, one additional convective layer due to the moderate-temperature silicate opacity peak, or even two additional separated convective layers due to moderate-temperature silicate and water-ice opacity peaks; the appearance of convective layers depends on how close to the optical surface the opacity peaks occur.

(b) *The Local Vertical Structure*

The local vertical structure is shown in Figs. 3a–3j for a representative solution with a midplane convective zone and a convective layer. The opacity in the convective layers is due primarily to water-ice grains while the convection at midplane is due primarily to moderate-temperature silicates. The specific heat is computed with the 3 : 1 *ortho* to *para* mixture of H_2 , which is reflected in the height dependence of ∇_{ad} in Fig. 3b. The averaging process of v_t is shown in Fig. 3d, in which we plot the locally calculated value of v_t with its surface density average; it is the density average that is actually used to compute the local vertical thermodynamic structure (see Sect. VI in Paper I). We have computed the local values of the turbulent velocity (v_t) from the thermodynamic structure and plotted them in Fig. 3i with their average value. *The average v_t in this example is about 1% of the average sound speed.* Note that the local values of v_t and v_i are peaked strongly in the outer region of the convection zone and decrease rapidly toward midplane, vanishing at $z = 0$.

In most models the midplane convection comprises a majority of the vertical structure in terms of height and mass. This property can be quantified in terms of the “fractional extent of the midplane convection,” defined as the ratio of the vertical extent of the midplane convection zone ($2z_c$) to the distance between optical surfaces ($2H$), and

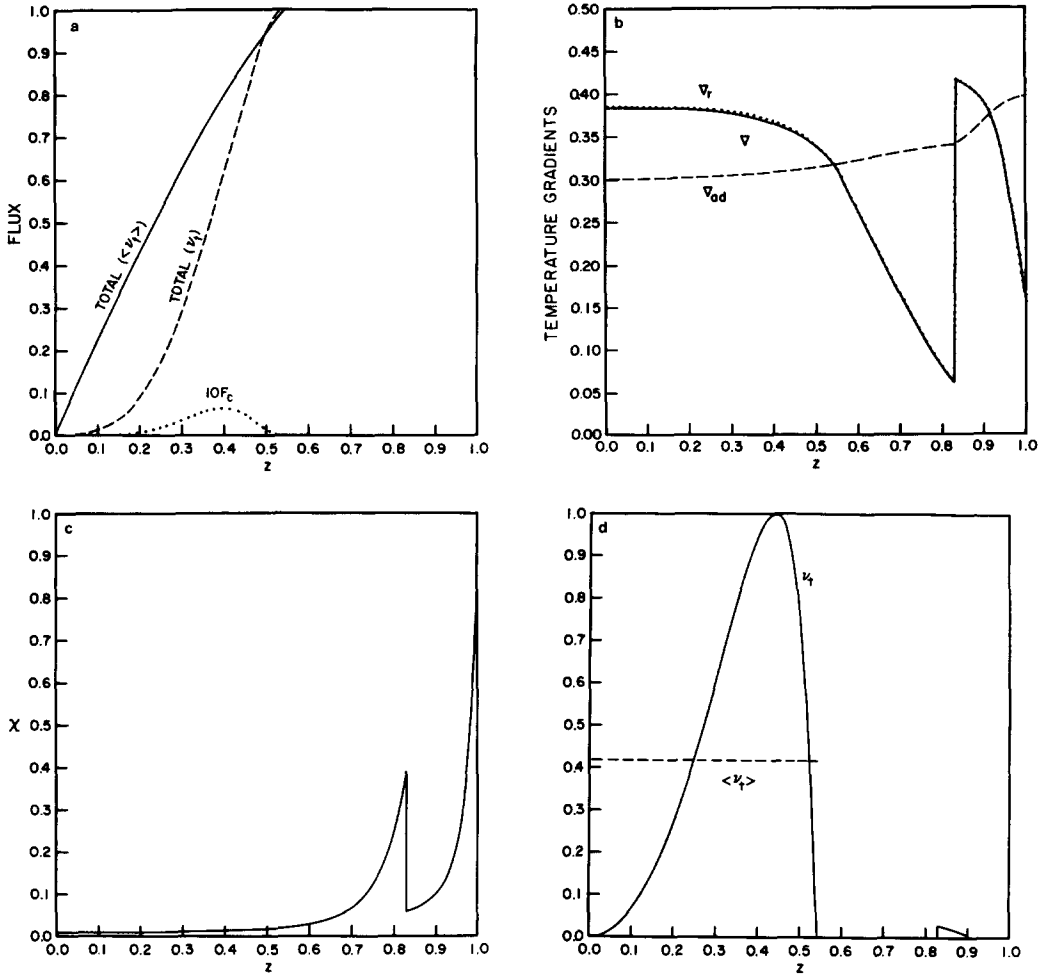


FIG. 3. (a–j) Vertical structure plots of various model parameters for the solar nebula accretion disk with $\log \dot{M} = 18.5$ (\dot{M} in g sec^{-1}) at $R = 4 \times 10^{13}$ cm, where R is the distance from the central object. The effective temperature is 61.2°K and the height above midplane H is 5.16×10^{12} cm. The abscissa for all the plots is z , the height above the midplane, normalized to the height of the optical surface, H . (a) The flux normalized to the surface value, $795 \text{ ergs sec}^{-1} \text{ cm}^{-2}$. Solid line is the total flux calculated with constant turbulent viscosity; dashed line is the total flux calculated with the local turbulent viscosity. The convective flux, multiplied by 10, is denoted by the dotted line. (b) The dimensionless temperature gradients, $(d \ln T)/(d \ln p)$. Solid line refers to the real gradient ∇ ; dotted line to ∇_r , the gradient if all the flux were carried by radiation only; dashed line to the adiabatic gradient, ∇_{ad} (see text, Sect. IV). (c) The radiative conductivity χ normalized to the maximum value, $4.35 \times 10^{16} \text{ cm}^2 \text{ sec}^{-1}$. (d) The local and averaged turbulent viscosities normalized to the maximum local value, $6.49 \times 10^{14} \text{ cm}^2 \text{ sec}^{-1}$. The averaged value of the viscosity, $2.72 \times 10^{14} \text{ cm}^2 \text{ sec}^{-1}$, is for the midplane convective layer only. (e) The temperature T , pressure p , and density ρ normalized to their respective central values: 281°K , 2.62 dyn cm^{-2} , $2.63 \times 10^{-10} \text{ g cm}^{-3}$; the opacity κ is normalized to the maximum value, $4.2 \text{ cm}^2 \text{ g}^{-1}$. (f) $S = \sigma \text{Ra}$ normalized to the maximum value, 3.16×10^5 . (g) The Rossby number Ro normalized to the maximum value, 0.755. (h) The growth rate $n(k_0)$ and the anisotropy factor α normalized to their respective maximum values, $6.89 \times 10^{-9} \text{ sec}^{-1}$ and 56.4. (i) The turbulent speed v_t and sound speed c_s , normalized to their respective maximum values, 448 and $1.2 \times 10^5 \text{ cm sec}^{-1}$. The averaged turbulent velocity values are denoted for each convective layer: 218 cm sec^{-1} for the midplane convective layer; 46 cm sec^{-1} for the off-midplane layer. (j) The local ratio of turbulent to sound speed v_t/c_s , normalized to the maximum value, 4.16×10^{-3} .

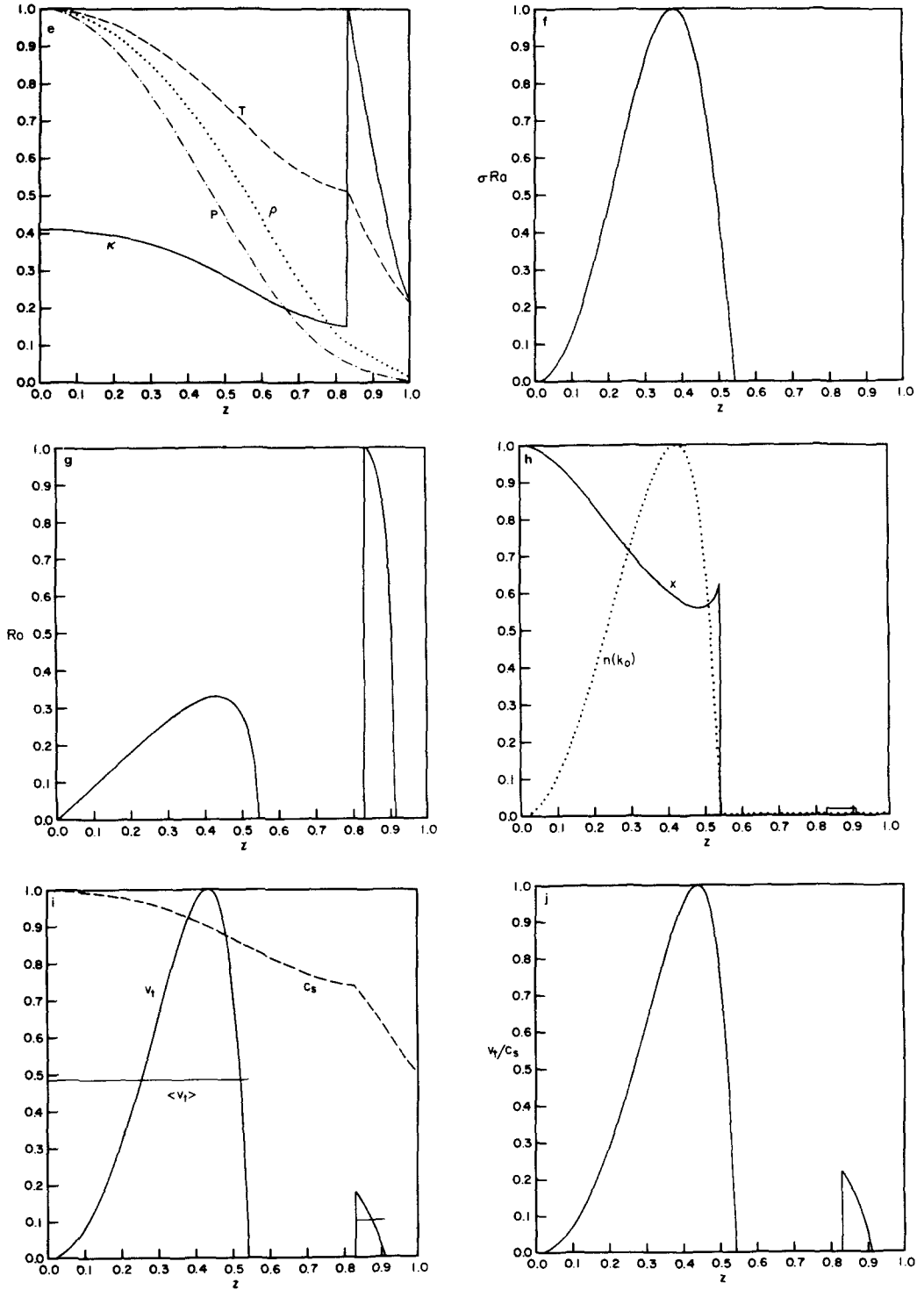


FIG. 3—Continued.

the “fractional mass of the midplane convection,” defined as the ratio of surface density in the midplane convection zone,

$$\Sigma_c = \int_{-z_c}^{z_c} \rho dz, \quad (19)$$

to the total surface density,

$$\Sigma = \int_{-\infty}^{\infty} \rho dz. \quad (20)$$

For models in which the opacity at midplane is near an opacity peak ($T_c \approx T_\kappa$), the fractional mass of the midplane convection is 0.85–0.95; the fractional extent of midplane convection here is about 0.85 in ice models, 0.80 in silicate models, and 0.75 in iron models. These fractions decrease as one moves down the opacity peaks with lower temperatures. When we decrease temperatures in the silicate and iron models to points where the convective layers are providing over 20% of the turbulent energy deposition, the fractional mass and extent of the midplane convection have decreased to about 0.70 and 0.45, respectively. (We stop computing silicate and iron models at these points because the additional iterations required by the convective layers become restrictive.) We compute cool ice models near the optically thin limit ($\tau_c \leq 2$), where the fractional mass and extent of the midplane convection decrease to about 0.30 and 0.45, respectively. Part of the reason that the fractional mass decreases to such a low value is because when $\tau_c = 2$, the surface density contained in the large radiative atmosphere is already 40% of the total surface density.

(c) Upper and Lower Temperature Bounds

For $T > T_\kappa^{\text{Fe}}$, the evaporation temperature of iron grains, effectively all grains evaporate at the densities encountered in the solar nebula models, and only the very low gas opacity remains. Because of the behavior described in Section IIa, we are unable to find consistent solutions with grain opacities for a given radius and effective temper-

ature when $T > T_\kappa^{\text{Fe}}$. In principle, we could construct models with gas (primarily hydrogen) opacities large enough to sustain midplane convection, but these models would need to be very thick and too hot to correspond to conditions generally assumed in the primordial solar nebula, having a greater resemblance to stellar conditions. We therefore take the consistent solutions for which $T_c = T_\kappa^{\text{Fe}}$ as the upper bound in effective temperature at a given radius. Figure 4a shows, for several radii, T_c vs T_e and the upper limits of T_c for the different types of midplane convection.

At some radii, the models become marginally optically thin ($\tau_c < 10$), at which point our assumption of radiative transport wholly by diffusion becomes invalid. Marginally optically thin models are seen for $R = 10^{13}$ and 10^{14} cm in Fig. 4b, showing τ_c vs T_e . When τ_c becomes less than 10, it drops dramatically as the convective elements become optically thin and their radiative dissipation rates reach an asymptotic maximum,

$$\delta_\chi = \frac{4ackT^3}{c_p}. \quad (21)$$

This causes the convective efficiency to increase with decreasing κ and T , contrary to the trend in optically thick disks, and thus resulting in comparatively thinner disks. As opacities become low enough in all types of midplane convection, much more material must be added to the vertical structure to produce a superadiabatic temperature gradient, eventually causing the optical depth to rise with decreasing T_e . At large enough radii (e.g., $R = 5 \times 10^{14}$ cm), τ_c turns up in the ice models without ever becoming optically thin. In this case there is no strict lower bound to constrain T_e , except by the empirical argument that molecular clouds have canonical temperatures of 10°K, such that models with $T < 10^\circ\text{K}$ may be excluded as unrealistic. The accretion rate in a steady disk is given by

$$\dot{M} = \frac{2\pi acT_e^4}{3\Omega^2} \quad (22)$$

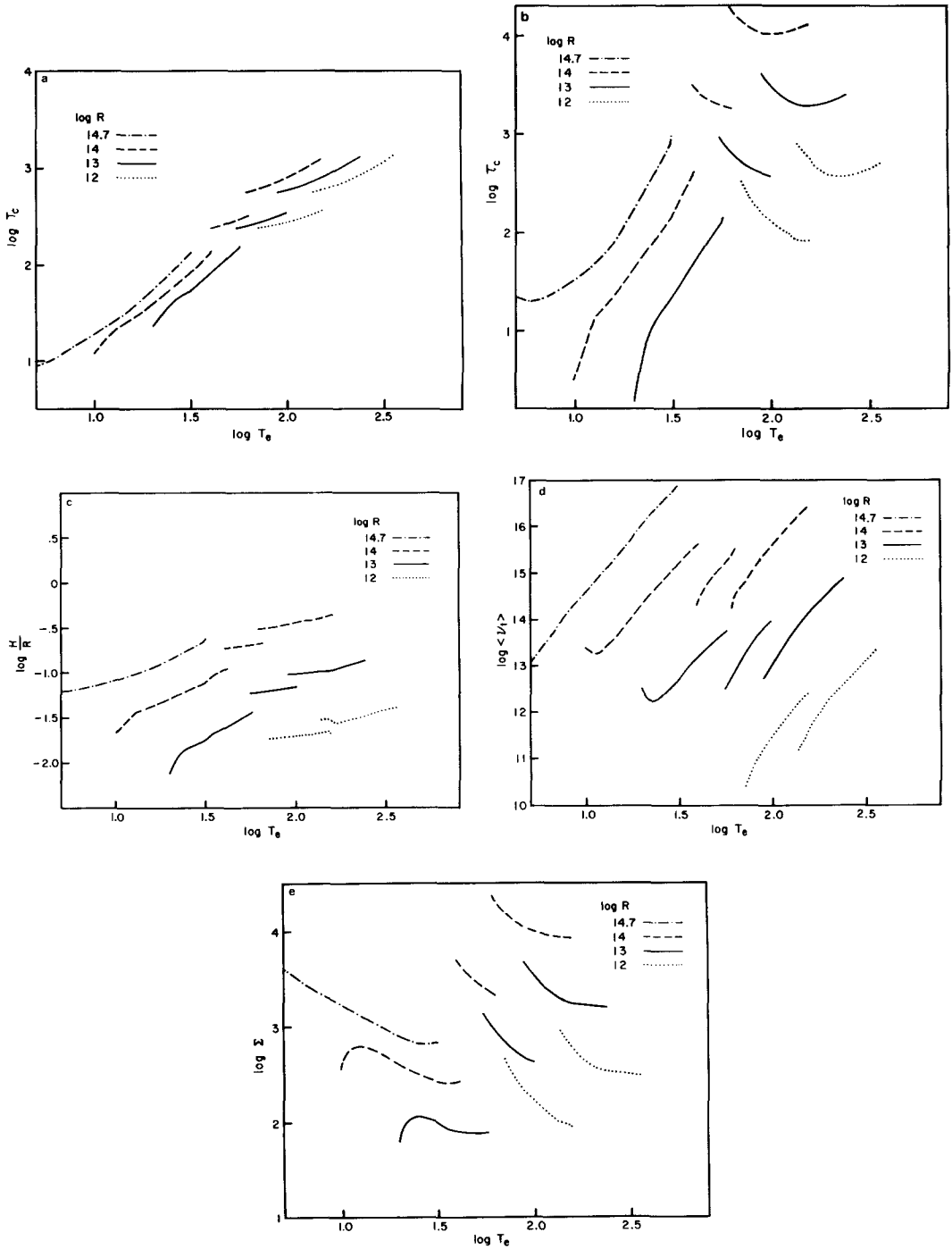


FIG. 4. Model parameters of the disk as a function of the effective temperature T_e for radii of $\log R = 12, 13, 14, 14.7$, where R is in cm. (a) The midplane temperature T_c in $^{\circ}\text{K}$. (b) The optical depth to midplane τ_c . (c) The ratio of the height of the optical surface H to radius R . (d) The average coefficient of viscosity $\langle \nu \rangle$ in $\text{cm}^2 \text{sec}^{-1}$. (e) The surface density Σ in g cm^{-2} .

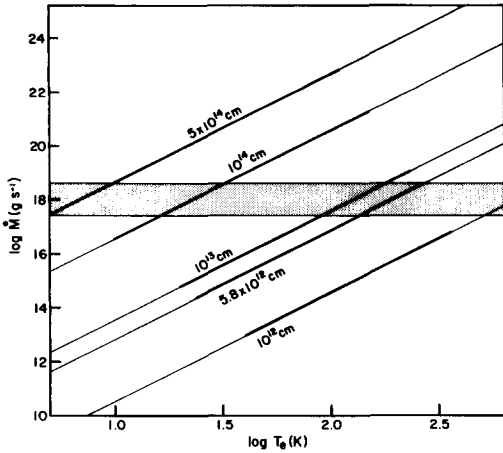


FIG. 5. The mass accretion rate \dot{M} as a function of effective temperature T_e for radii ranging over the extent of the present solar system. The dark lines denote models with valid solutions. The region between the horizontal lines represents the common range in \dot{M} for which a constant accretion rate exists for R ranging from 5.8×10^{12} to 5.0×10^{14} cm.

at radii much larger than the central object's radius (Pringle, 1981).

The largest allowed T_e at Mercury's orbit (266°K at $R = 5.8 \times 10^{12}$ cm) corresponds to a maximal accretion rate \dot{M} of $10^{18.5}$ g sec $^{-1}$. In order to constrain $T_c > 10^\circ\text{K}$ for an orbit between Neptune and Pluto of $R = 5 \times 10^{14}$ cm, we require $\dot{M} > 10^{17.5}$ g sec $^{-1}$. This narrow range of allowed accretion rates for a stationary disk spanning the present solar system is shown in Fig. 5 on an $\dot{M} - T_e$ diagram with the allowed ranges of models having midplane convection.

(d) General Properties of the Models in T_e and R

We have computed vertical structures for selected effective temperatures at radii of 10^{12} , 10^{13} , and 10^{14} cm in order to examine general properties of the solutions. We have also computed a limited number of models at radii corresponding to the present orbits of Mercury (5.79×10^{12} cm) and Neptune-Pluto (5×10^{14} cm). The gross properties of the solutions are plotted in Figs. 4a-4e. The central (midplane) tem-

perature T_c , the optical depth to midplane τ_c , the ratio of the height of the optical surface H to radius R , the density-averaged coefficient of turbulent viscosity $\langle \nu_t \rangle$, and the surface density Σ are shown against T_e in Figs. 4a-4e, respectively, for different radii and different types of midplane convection. The dimensionless coefficient of turbulent viscosity after Pringle (1981),

$$\alpha_c = \langle \nu_t \rangle \frac{\rho_c}{p_c} \Omega, \quad (23)$$

the central density ρ_c , and the central pressure p_c are shown against T_c in Figs. 6a-6c, respectively.

The primary feature of the models is the steep dependence of the turbulent viscosity on T_e and T_c . This is mainly due to the decline in opacity with falling temperatures, making it more difficult for a superadiabatic temperature gradient to be sustained. In order to counter the decline in opacity and turbulent energy generation rate, the disk must have more material present to produce a given amount of radiant flux; this results in the general increase in surface density and central density with decreasing temperature. This effect is also reflected in the optical depth to midplane, especially in the iron and silicate models. Note that the values of T_c in the iron and silicate models approach an asymptotic minimum with decreasing T_e in Fig. 4a. Note also that the central pressures have nearly uniform values for a given radius and type of midplane convection.

The aspect ratio H/R generally increases monotonically with T_e in Fig. 4c, except for a small inversion near $\log T = 2.1$, especially evident in models for $R = 10^{12}$ cm. This is caused by the condensation of water ice in the atmosphere near the optical surface, which changes the optical surface boundary condition Eq. (14).

Only solutions with the standard 3:1 mixture of *ortho* to *para* H_2 and Pollack grain opacities are plotted in these figures. A comparison of heights of the optical surface and surface density for different mix-

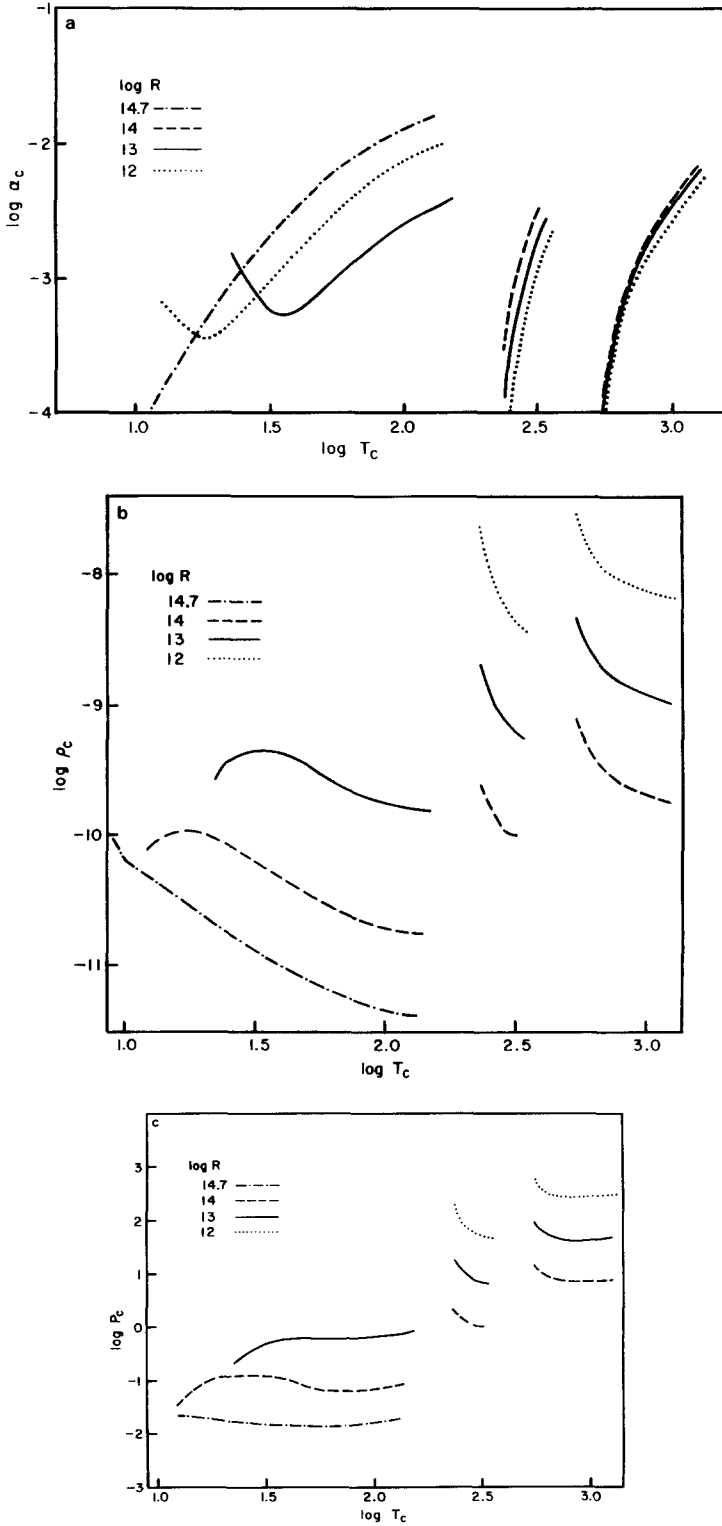


FIG. 6. Model parameters of the disk as a function of the central (midplane) temperature T_c , for $\log R = 12, 13, 14, 14.7$. (a) The turbulence coefficient α_c , as defined in Eq. (23) (Sect. IV). (b) The central density ρ_c in g cm^{-3} . (c) The central pressure P_c in dyn cm^{-2} .

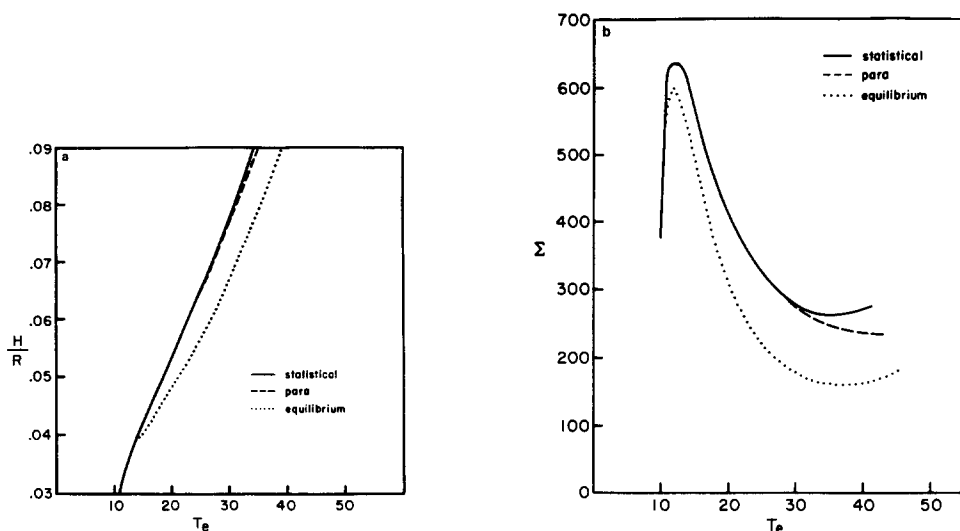


FIG. 7. A comparison of low-temperature ice models vs T_e calculated at $\log R = 14$ using the three possible mixtures of *para* and *ortho* H_2 . (a) The height of the disk (H in units of R). (b) The surface density Σ in g cm^{-2} .

tures of *para* and *ortho* H_2 in low-temperature ice models is shown in Figs. 7a and 7b. A sample comparison between solutions with DeCampli–Cameron opacities and Pollack opacities is shown in Figs. 8a–8c for silicate and iron models. The DeCampli–Cameron opacities are larger than the Pollack opacities and have a higher temperature dependence in this temperature range, both of which cause the models with DeCampli–Cameron opacities to be thinner and have higher average viscosities than models with Pollack opacities. The two opacities give very similar solutions at low temperatures where water ice dominates the opacities.

(e) Radial Properties of Steady Disk Models

The maximal accretion rate for a steady disk with radii spanning the planetary orbits and with a central mass of $1M_\odot$ is about $10^{18.5} \text{ g sec}^{-1}$ (see above). We have ordered vertical structures for constant values of \dot{M} of 10^{18} , $10^{18.5}$, and $10^{19} \text{ g sec}^{-1}$ in order to show the sensitivity of the steady disk models to \dot{M} . At the regions of overlapping

solutions between ice and silicate midplane convection and silicate and iron midplane convection, we have artificially connected the solutions to correspond to a minimum of disk mass. Specifically, we follow the ice models from the outermost radii until midplane temperatures are too high to allow midplane convection with water-ice opacities. At that point, we switch to silicate models and decrease the radius until midplane convection is no longer possible with moderate-temperature silicate opacities. Finally, we switch to the iron models and proceed to an innermost radius where all grains evaporate. As discussed above, finite transition regions must actually occur with large radial gradients for which our governing assumptions are invalid. We display the radial behavior of the steady disk models in Figs. 9a–9h only out to a radius of $10^{14.5} \text{ cm}$, at which point the disk's self-gravity becomes important and the Jean's criterion (33) for gravitational instability becomes marginally satisfied. Although we have calculated the structure with convective turbulence beyond this radius (see Table I), the governing equations become in-

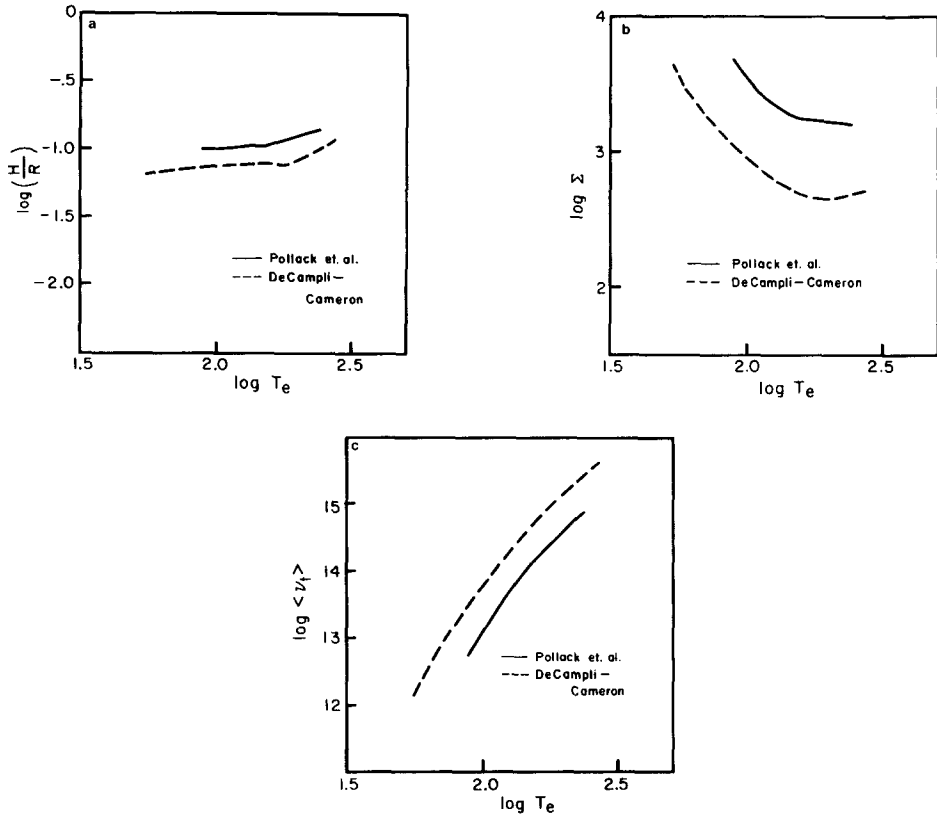


FIG. 8. A comparison of high-temperature silicate and iron models vs T_c calculated at $\log R = 13$ using the two different opacities. Solid line refers to the models using the opacities of Pollack *et al.* (1986); dashed line refers to the opacity of DeCampli and Cameron (1979). (a) H/R . (b) Σ in g cm^{-2} . (c) $\langle \nu_t \rangle$ in $\text{cm}^2 \text{sec}^{-1}$.

valid. In Figs. 9, we show the radial behavior, respectively, of the aspect ratio H/R , the surface density Σ , and the optical depth to midplane τ_c ; the central temperature T_c , density ρ_c , and pressure P_c ; and the turbulent viscosity coefficients $\langle \nu_t \rangle$ and α_c . The positions of the planets are marked in Fig. 9a for reference.

Figure 9a shows that H/R is roughly $\frac{1}{10}$ for all models, being larger for larger M . The iron and silicate models at smaller radii have larger values of H/R and a greater amount of flaring than do the ice models at the largest radii. The kink in the iron models is due to water-ice condensation near the optical surface, causing rapid changes in the surface boundary condition.

While the mean surface density decreases from iron to ice models with increasing radius, the surface density within a type of model always increases, as seen in Fig. 9b. This is caused by the rapid decline of turbulent energy generation rates with increasing radius for a given type of midplane convection, as seen in Figs. 9g and 9h. While τ_c reflects the behavior of Σ in the iron and silicate models, it decreases with increasing R in the ice models, since the decline in $\langle \nu_t \rangle$ and α_c is less steep in the ice than in the iron and silicate models.

The central temperature decreases monotonically with increasing radius for a given type of midplane convection and between types of models (Fig. 9d). However,

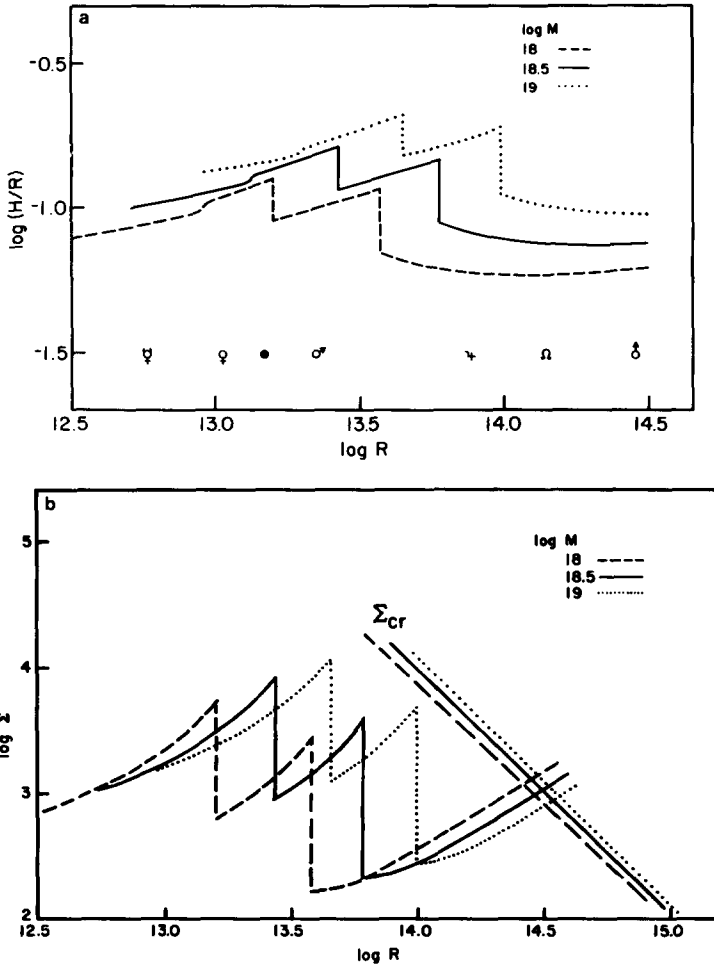


FIG. 9. (a–h) Model parameters of the disk as a function of the radius R from the central mass of $1M_{\odot}$. Curves are for three different accretion rates, $\log \dot{M} = 18, 18.5, 19$ (\dot{M} in g sec^{-1}). (a) The height of the disk above midplane H normalized to R (in cm). (b) The surface density Σ in g cm^{-2} . The lines at $\log R = 14.5$ denote the value of the surface density at which the disk becomes gravitationally unstable (see text, Sect. V). (c) The optical depth to midplane τ_c . (d) The temperature at midplane T_c in $^{\circ}\text{K}$. (e) The density at midplane ρ_c in g cm^{-3} . (f) The pressure at midplane P_c in dyn cm^{-2} . (g) The averaged turbulent viscosity $\langle \nu_t \rangle$ in $\text{cm}^2 \text{sec}^{-1}$. (h) The turbulence coefficient α_c as defined in Eq. (23) (Sect. IV).

the central density and pressure in Figs. 9e and 9f show a plateau effect from one type of midplane convection to another, in most instances decreasing with increasing radius at the hot end of a given type of midplane convection, then increasing at the cool end as convection becomes less efficient. In fact we note that the steady models for convective turbulence can be quite accurately approximated as connected isopycnic models.

(f) *The Effect of Different Central Masses*

We have initially assumed that the proto-sun in the center of the primordial solar nebula contains its present mass. However, because the convective models violate Jean's criterion in the outer Jovian orbits, there must be a significant amount of mass contained in the disk. If we still insist on a central mass of $1M_{\odot}$, then we must invoke a

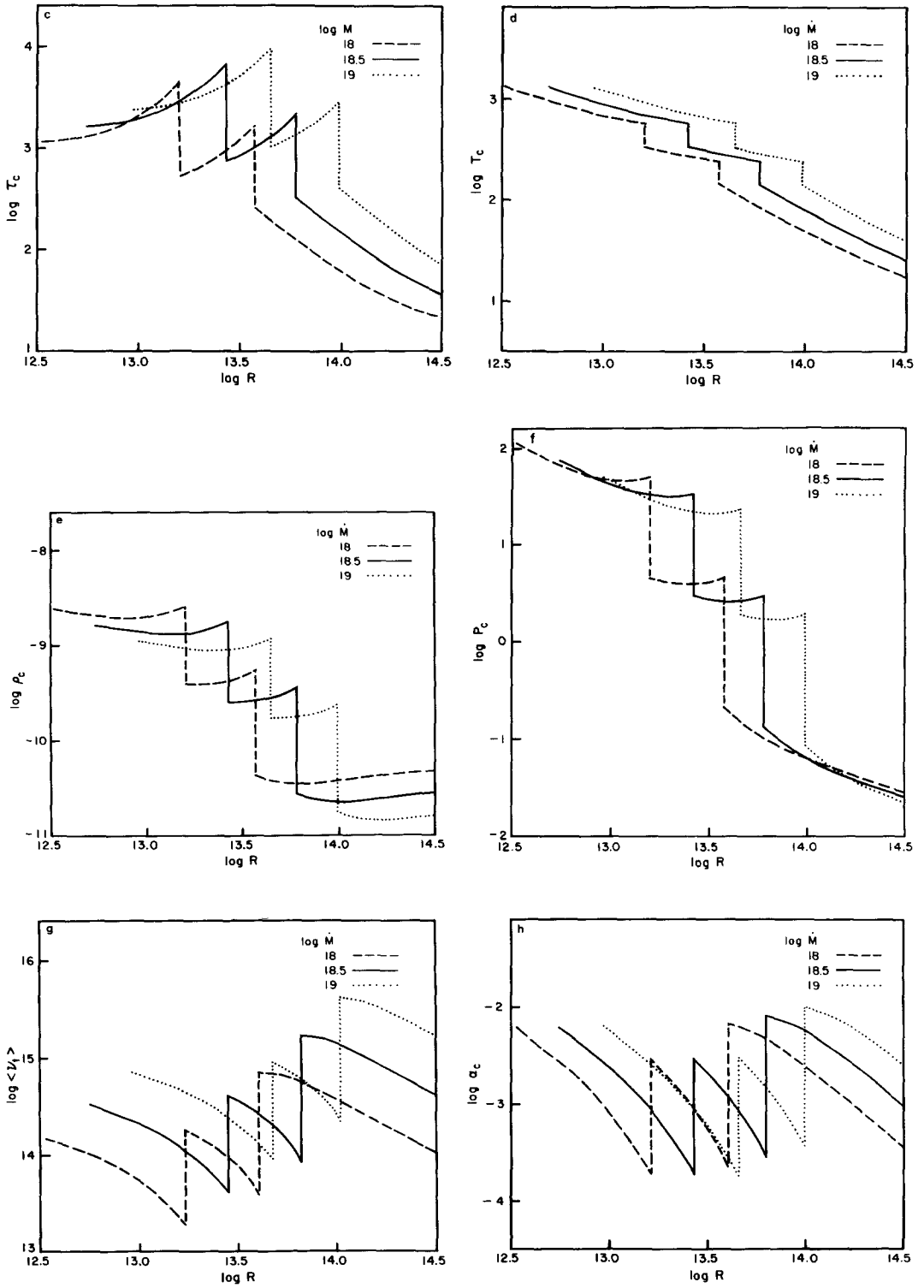


FIG. 9—Continued.

TABLE I

log R	log Σ	log T_c	log ρ_c	log τ_c	log χ_c	log $\langle v_t \rangle$	log S	Ro	x	log $n(k_0)$	log (v_t/c_s)	log α_c
12.750	3.023	3.115	-8.792	3.218	14.739	14.516	4.882	0.342	32.6	-6.782	-1.916	-2.21
13.100	3.340	2.895	-8.888	3.351	14.501	14.225	5.426	0.264	60.8	-7.395	-2.226	-2.81
13.431	3.885	2.762	-8.772	3.818	13.963	13.668	6.601	0.117	198.9	-8.247	-2.310	-3.73
								0.509				
								0.435				
13.435	2.944	2.523	-9.602	2.871	14.892	14.631	5.153	0.328	37.6	-7.790	-2.069	-2.53
								0.425				
13.600	3.175	2.449	-9.581	3.042	14.682	14.434	5.500	0.249	56.4	-8.162	-2.381	-2.90
								0.755				
13.784	3.535	2.383	-9.464	3.341	14.326	14.070	6.043	0.176	105.6	-8.608	-1.916	-3.48
								0.881				
13.800	2.324	2.136	-10.406	2.484	15.448	15.237	4.694	0.494	21.3	-8.154	-1.721	-2.09
14.100	2.540	1.795	-10.650	2.022	15.233	15.060	4.973	0.383	28.3	-8.714	-2.033	-2.37
14.600	3.160	1.314	-10.536	1.500	14.749	14.500	5.776	0.197	75.4	-9.701	-2.691	-3.20
15.000	3.731	1.042	-10.425	1.565	14.271	13.457	6.859	0.095	310.7	-10.541	-3.361	-4.07

Note. The values of T_c , ρ_c , τ_c , and χ_c are those at midplane. The values of S , x , $n(k_0)$, and v_t/c_s correspond to the maximum values for the midplane convective layer only. The maximum Rossby number for each convective layer in a vertical structure model is presented with the midplane value listed first and the outer-most listed last. The turbulence coefficient α_c , is calculated by using Eq. (23); all values (in cgs units) are for log $M = 18.5$.

mechanism for mass loss from the central region of the solar nebula. Alternately, we can assume that the sum of the mass in the primordial sun and disk is $1M_\odot$. We cannot accurately determine the amount of mass in the disk model, since most of the mass is contained in the outer region of the disk precisely where self-gravity becomes important and the convective model becomes inappropriate. Likewise, the central mass is ill determined, and so it is of interest to determine the behavior of our models for different values of the central mass. In the following discussion, we shall be biased toward central masses less than $1M_\odot$.

The central mass M (assumed much greater than the disk's mass) enters the calculation through the gravitational potential; and in the thin-disk approximation one equates Ω^2 with GM/R^3 . Therefore, varying M is equivalent to varying Ω . The radius also only appears explicitly in the expression for Ω . Thus, a family of solutions exists for a given value of Ω with radius given

by $R^3 = GM/\Omega^2$. We let R_1 be the radius assigned to base computations with $M = 1M_\odot$. Radial solutions for different M are obtained simply by assigning $1M_\odot$ solutions with $R_1 = m^{-1/3}R$ to R , where $m \equiv M/M_\odot$. In Figs. 9a-9h, this corresponds to shifting the scale of log R (which is really log R_1) on the abscissa by $-\frac{1}{3} \log m$; e.g., for $m = 0.5$ the log R scale is shifted to the right by about 0.1.

The maximal accretion rate is determined by the hottest iron model allowed at Mercury's orbit. One can see from the figures and the preceding argument that decreasing M allows larger values of the maximal accretion rate. The maximal M goes empirically as $R_1^{2.25}$, or $m^{-0.75}$. However, it would still take m as low as 0.2 to allow an accretion rate of greater than 10^{19} g sec $^{-1}$.

The maximal accretion rate by this method of calculation may be more sensitive to m than this. If protomercury, or its constituents, was formed from the nebula when M was less than $1M_\odot$, and if the spe-

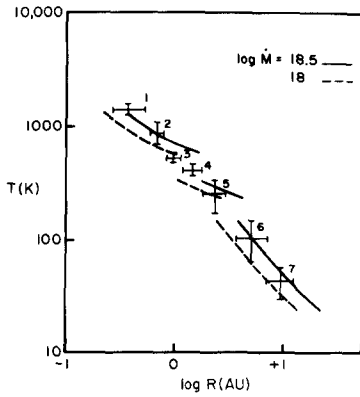


FIG. 10. The calculated central temperatures T_c vs R for $\log \dot{M} = 18$ and 18.5 are compared to the data by Lewis (1974) (crosses).

cific angular momentum, $(GMR)^{1/2}$, was approximately conserved, then the conditions relevant to present-day Mercury occurred at a more distant radius, $R/R_\oplus = M_\odot/M$. In this case, the grain evaporation criterion at Mercury should be applied for a central mass M to the $1M_\odot$ solution at $R_1 = R_\oplus m^{-4/3}$, hence the maximal \dot{M} would scale as m^{-3} . If the protosun accreted a substantial fraction of its mass during or after planet formation, much higher accretion rates may be applicable in the solar nebula.

(g) Comparison with Characteristics of the Solar System

The composition of the terrestrial planets and Jovian satellites gives information on the temperatures at which planetesimals formed in the primordial solar nebula. In Fig. 10, we compare these estimated temperatures (Lewis, 1974) with the midplane temperatures that we obtain with $\dot{M} = 10^{18}$ and $10^{18.5}$ g sec⁻¹. Our results agree quite well with the data points; however, the necessity of fitting points 1 to 5 and 6 and 7 simultaneously is perhaps not stringent. Points 1 to 5 are obtained from terrestrial planets and an asteroid. Points 6 and 7 are obtained from satellites of Jupiter and Saturn, and so may belong to an epoch of

planetesimal formation different from points 1 to 5.

The run of surface density in models of the primordial solar nebula can be compared with the "minimum mass" distribution of the solar system; this is computed by augmenting the masses of the present planets and asteroids to solar elemental abundances and smearing them between their orbits. Aside from a gap in the asteroid belt, the minimum mass distribution gives a surface density that falls roughly as $R^{-3/2}$ (Weidenschilling, 1977). In Fig. 9b, we see for the convective models an overall tendency for Σ to decrease with R from iron to ice midplane convection. However, the surface density for a given type of midplane convection increases with R . It is therefore difficult to find a direct correspondence between the run of surface density in the convective model and for the minimum mass distribution. At the radii of the outer Jovian planets we expect Σ to turn over and decrease with R because of gravitational instability (Sect. VI), but this only forms a lobelike distribution of surface density (Fig. 11).

The present convective models inevitably lead to massive disks in which self-gravity becomes important. The mass of the

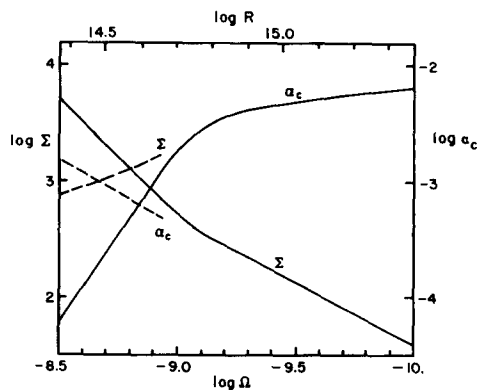


FIG. 11. The surface density Σ and turbulence coefficient α_c for vertical gravitational collapse (solid lines) vs R (or Ω in sec⁻¹) for $\log \dot{M} = 18.5$, $\gamma = \frac{3}{2}$, $\xi = 2$, $\kappa_0 = 1.5 \times 10^{-4}$ cm² g⁻¹. The dashed lines correspond to a convective disk model.

steady disk interior to a radius R and exterior to the radius R_{\min} where grains are first able to condense is given by

$$M_d = \int_{R_{\min}}^R 2\pi\Sigma(R')R'dR'. \quad (24)$$

Most of the disk's mass resides at the outer Jovian orbits and since Σ is approximately proportional to $R^{1.25}$, $M_d(R) \approx 2\Sigma(R)R^2$. The point where the disk becomes gravitationally unstable, i.e., where $\Sigma = \Sigma_{\text{cr}}$, Eq. (33) corresponds to

$$M_d(R)/M \sim 2h/R. \quad (25)$$

Therefore the ratio of the (interior) disk mass to central mass M at Σ_{cr} is around 0.1 to 0.2, and the ratio is probably increased several tenths more in the self-gravitating region beyond Σ_{cr} , as suggested by the run of surface density for marginal gravitational instability (Fig. 11). Since a fair fraction of a solar mass is contained in the disk model, the appropriate value of the mass of the central protosun is uncertain. If a mass loss mechanism operates, such as bipolar ejection, the mass of the central body could be near its present value; if not, then only a fraction of a solar mass could be appropriately assigned to the central body. This problem needs more extensive analysis.

Within the present model, the characteristic dissipation time for the solar nebula is given by

$$\tau_d = \frac{M_d}{\dot{M}} \approx 20 \left(\frac{M_d}{M_{\odot}} \right) \text{myr} \quad (26)$$

for $\dot{M} = 10^{18.5} \text{ g sec}^{-1}$. We expect M_d to be several tenths of M_{\odot} ; thus, τ_d should be on the order of 10 myr.

Gravitational instabilities operating in the outer disk may lead to inconsistencies with popular hypotheses of Jovian planetary formation. This situation suggests that a "gas instability" could be responsible for the formation of the outer planets rather than a "core instability"; however, the former mechanism fails to account for the size dis-

tribution of the rocky cores of the outer planets (Pollack, 1984; D. J. Stevenson, private communication, 1986).

V. THE STABILITY OF STEADY DISK MODELS

In this section we discuss the radial properties of disks with constant accretion rate spanning the orbits of the present planets. These steady disk models are constructed by ordering by radius a sequence of vertical structure solutions which satisfy Eq. (22) (Sect. 6) with a given \dot{M} . Such a steady disk can only be realized in nature over a certain radial extent provided material is supplied to it at the outer radial boundary at a steady rate and removed at the same rate at the inner radial boundary. While this situation can readily occur in close binaries with steady mass transfer, it may only hold in a transitory sense in the primordial solar nebula, since the nebular material is constantly being depleted and eventually must run out. In a thick cloud, material may also enter the inner disk region almost vertically and perhaps inhomogeneously, admitting the possibility of an approximately stationary disk with an \dot{M} that varies with radius. Further, the behavior of the vertical structure solutions with radius, assuming that convection is the sole source of turbulent viscosity, may make the realization of a steady disk difficult, which we discuss at length below. The properties of steady disks described in the previous section may be appropriate to only limited spatial regions and only episodically in the history of the solar nebula.

(a) Radial Condensation Boundaries

The high-temperature end of the ice models and the low-temperature end of the silicate models, as well as the high-temperature end of the silicate models and the low-temperature end of the iron models, have overlapping solutions for some values of T_c and R , leading to an ambiguity in the appropriate values of H , Σ , etc. The transition between models with different types of midplane convection cannot occur abruptly at some radius, for it would result in very

large radial gradients, clearly invalidating our governing assumptions. It is possible that solutions in the transition regions with significant radial gradients are time dependent or inherently unstable, which could inhibit any steady transfer of material from one region to another.

(b) Multivalued Solutions

A further complication arises in that the same value of Σ can occur at a given radius for different values of T_e . For instance, the high-temperature end of the ice models features an inversion in Σ , resulting in multiple values of T_e for certain values of Σ . Also, the low-temperature end of the silicate models shares values of Σ with the high-temperature end of the iron models at a given radius. Bath and Pringle (1985) suggested that this situation could lead to a limit cycle behavior in the disk, switching between low- and high-viscosity states.

(c) Viscous Diffusive Instability

Another question of stability lies in the general tendency of the surface density to decrease with increasing T_e . The mass transfer term

$$\mu \equiv \langle v \rangle \Sigma = \dot{M}/3\pi \quad (27)$$

is proportional to T_e^4 via the energy equation (6). Lightman and Eardley (1974) found that when $d\mu/d\Sigma < 0$ at a fixed radius, the disk is unstable to localized radial perturbations. The reason this occurs is that, when Σ is locally increased (decreased) by a small amount, the local mass transfer rate, proportional to μ , decreases (increases) commensurately when $d\mu/d\Sigma < 0$; this causes material to accumulate (disperse) more, and so leads to a runaway process. Thus the disk has the tendency to form rings, or perhaps clumps for nonaxisymmetric perturbations, when Σ depends on T_e as in Fig. 4e. The manner in which such instabilities in turn affect the properties of turbulence and the structure of the disk is not clear; in particular it is not

known if this diffusive instability precludes the formation of a steady disk entirely.

In calculating the growth behavior of the viscous diffusive instability, one assumes a disk with Keplerian rotation that is in vertical hydrostatic and thermal equilibrium. The linearized, time-dependent perturbation equation for the radial disk structure is given by (Pringle, 1981)

$$\frac{\partial m}{\partial t} = \frac{3}{4} \frac{m'(r)}{r^2} \frac{\partial^2 m}{\partial r^2}, \quad (28)$$

where $r = R^{1/2}$, $m = r\delta\mu$, and $m'(r) = (\partial\mu/\partial\Sigma)_r$. With separation of variables, one finds $m(r,t) = e^{nt}f(r)$, where n is the integration constant and growth/damping rate of the instability, and where $f(r)$ is governed by

$$\frac{d^2f}{dr^2} - \frac{4nr^2}{3m'(r)}f = 0. \quad (29)$$

Consider the boundary value problem for which $f(r)$ vanishes at two bounding radii, $f(r_1) = f(r_2) = 0$: then n is real and given by

$$n \int_{r_1}^{r_2} \frac{(rf)^2}{m'(r)} dr = -\frac{3}{4} \int_{r_1}^{r_2} \left(\frac{df}{dr}\right)^2 dr. \quad (30)$$

Thus n has the opposite sign of the average inverse m' . If $m' > 0$ everywhere in the domain between r_1 and r_2 , then $n < 0$ and the perturbation is damped (stable); if $m' < 0$ somewhere in the domain, then n can be positive and the perturbation is growing (unstable). For some regions of the steady (constant \dot{M}) disk models, m' can be approximated by a power law going as r^{-p} . In this special case, the solution of Eq. (29) for $p \neq -4$ is

$$f(r) = r^{1/2} B_{1/2q} \left[\left(\frac{4n}{3m'} \right)^{1/2} \frac{r^2}{q} \right], \quad (31)$$

where $B_{1/2q}$ is a Bessel function of order $1/2q = 1/(p+4)$. The eigenvalues of n are approximated by

$$n_l \approx -\frac{3}{4} m' \left(\frac{\pi l q}{r^2} \frac{r^q}{r_2^q - r_1^q} \right)^2, \quad l = 1, 2, 3, \dots, \quad (32)$$

which is roughly a radial average of the viscous diffusion rate ν_i/R^2 multiplied by $(-\partial \ln \dot{M}/\partial \ln \Sigma)$, and a radial wavenumber squared. The radial structure is unstable at all wavelengths with the shortest wavelength modes growing most rapidly. Once the perturbations reach finite amplitude, the radial structure begins to depart significantly from thermal equilibrium, radial thermodynamic gradients become important, and the governing equation (28) for the growth of the instability becomes invalid.

(d) Jean's Instability

The self-gravity of the disk becomes important for the outer Jovian orbits, and a trial steady disk structure may prove to be unstable to gravitational collapse. The Jean's criterion for gravitational instability is given roughly by

$$\Sigma > \Sigma_{\text{cr}} \equiv \frac{hM}{R^3}, \quad (33)$$

where $h \equiv (p/\rho\Omega^2)^{1/2}$, evaluated at mid-plane, is the isothermal scale height (Pringle, 1981; Safronov, 1969; also compare Eq. (2), Sect. II). For a typical aspect ratio h/R of about 0.1 and $M = 1M_\odot$, the critical surface density at $R = 10^{14}$ cm is about 2×10^4 g cm $^{-2}$. Comparing this with Fig. 4e shows that only some hot iron models at $R = 10^{14}$ cm marginally satisfy condition (33). At $R = 5 \times 10^{14}$ cm, however, $\Sigma_{\text{cr}} \approx 800$ g cm $^{-2}$, such that all models are at least marginally unstable to gravitational collapse.

In Fig. 9b the critical surface density is estimated at the outer radii of the solar nebula and compared with values of Σ from steady models. It is seen that for $R > 3 \times 10^{14}$ cm, condition (33) is satisfied and the Jean's instability should occur. The surface density increases with increasing radius in the outer Jovian orbits, which causes the amount of mass in the disk interior to a fixed radius to be larger for a smaller central mass (see Sect. IVf). This causes the radius at which the Jean's criterion (33) is first satisfied (R_j , say) to be *smaller* for a

smaller central mass at a fixed accretion rate. consider the dependence of R_j on m for a constant \dot{M} . For $m \equiv M/M_\odot = 1$, we find $\Sigma \sim R^s$ with $s = 1.25$ at Jovian orbits; for arbitrary m , $\Sigma \sim R^s m^{-s/3}$. We let h/R in criterion (28) be approximately a constant in R ; thus,

$$\Sigma_{\text{cr}} \equiv \frac{Mh}{R^3} \sim mR^{-2},$$

$$R_j \sim m^{(s+3)/(3(s+2))} \sim m^{0.44}. \quad (34)$$

The dependence of R_j on m is somewhat less steep when \dot{M} is held at its maximum, since h/R increases and Σ decreases with increasing \dot{M} . We find that at the Jovian orbits, $h/R \sim \dot{M}^{0.19}$, $\Sigma \sim \dot{M}^{-0.28}$, $R_j^{s+2} \sim \dot{M}^{0.47}$. Using the prior result that the maximal \dot{M} goes as $m^{-4/3}$ and $s = 1.25$, we find $R_j \sim m^{0.33}$. Therefore, as the central mass increases, the boundary of gravitational instability generally recedes. However, if maximal \dot{M} scales as steeply as m^{-3} , as discussed in Section IVf, then R_j becomes almost independent of m .

It is possible that the effects of self-gravity in this region lead to a natural way of truncating the inner disk from the remnant protostellar cloud. It is also possible that Jean's unstable material becomes turbulent under collapse and enhances disk accretion as envisaged by Paczynski (1978). The answer to such speculations lie, however, in models that take explicit account of the disk's self-gravity. We may conclude, in any event, that the outermost region of the solar nebula cannot evolve to a state like that in our convective models.

VI. THE EFFECT OF SELF-GRAVITY ON RESULTS OF PRESENT WORK

For very short wavelengths, the growth rate $n(k)$ for gravitational collapse with radiative dissipation is governed by the quintic equation

$$n^5 + \gamma\chi k^2 n^4 + (k^2 c_s^2 + \Omega^2 - \omega_G^2) n^3 + \chi k^2 [k^2 c_s^2 + \gamma(\Omega^2 - \omega_G^2)] n^2 + [(k^2 c_s^2 - \omega_G^2) k_z^2 \Omega^2 k^{-2} - g\alpha\beta k_r^2 c_s^2] n + (k^2 c_s^2 - \gamma\omega_G^2) \chi k_z^2 \Omega^2 = 0, \quad (35)$$

where γ is the ratio of specific heats, χ the coefficient of radiative diffusion, c_s the sound speed, and $g\alpha\beta$ the convective lapse rate squared.

For *very short wavelengths* the self-gravity of the perturbation is given by

$$\omega_G^2 = \omega_0^2 \equiv 4\pi G\rho. \quad (36)$$

For *longer wavelength* radial perturbations, Safronov (1969, 1980) suggests the approximate form

$$\omega_G^2 = \omega_0^2 kh/(1 + kh), \quad (37)$$

where h is the characteristic half-thickness of the disk. The general condition for gravitational instability is

$$\omega_G^2 > \gamma^{-1} k^2 c_s^2. \quad (38)$$

For ω_G^2 slightly larger than $\gamma^{-1} k^2 c_s^2$, the growth rate is a combination of convective and gravitational instabilities. For $\omega_G^2 \gg k^2 c_s^2$, the growth rate is dominated by the gravitational instability, with $n(k) \approx \omega_G$. In the absence of buoyancy, the fastest growing modes occur for a *vertical collapse*, $k_r = 0$, for which the fifth-order Eq. (35) separates into

$$(n^2 + \Omega^2)[n^3 + \gamma\chi k^2 n^2 + (k^2 c_s^2 - \omega_G^2)n + \chi k^2 (k^2 c_s^2 - \gamma\omega_G^2)] = 0. \quad (39)$$

For radial collapse, $k_z = 0$, Eq. (35) becomes instead

$$n^2[n^3 + \gamma\chi k^2 n^2 + (k^2 c_s^2 + \Omega^2 - \omega_G^2)n + k^2[k^2 c_s^2 + \gamma(\Omega^2 - \omega_G^2)]] = 0, \quad (40)$$

where the cubic part is the standard expression for gravitational growth rates with radiative dissipation in an infinitesimally thin disk (Morozov *et al.*, 1985; Safronov, 1980).

For optically thick perturbations, the radiative dissipation rate of the perturbation is given by χk^2 . In the optically thin limit, the result changes to $3(\kappa\rho)^2\chi$. Unno and Spiegel (1966) join the two limits with the expression

$$\delta_\chi \equiv \chi k^2 \frac{3(\kappa\rho)^2}{3(\kappa\rho)^2 + k^2}. \quad (41)$$

In order to generate a gravitational instability, ω_0 (i.e., ρ) must be sufficiently large with respect to the acoustic frequency, but in order to accomplish this the growth rate must be small with respect to ω_0 in order to give a low-viscosity, high-density disk. We therefore expect the growth rate to be governed by the marginal state. The growth rate for vertical collapse is then, from Eq. (39),

$$n \approx \delta_\chi \frac{\gamma\omega_G^2 - k^2 c_s^2}{k^2 c_s^2 - \omega_G^2}, \quad (42a)$$

with ω_G^2 given by (36) and δ_χ by (41). Analogously, the growth rate for radial collapse is given by Eq. (40):

$$n \approx \delta_\chi \frac{\gamma(\omega_G^2 - \Omega^2) - k^2 c_s^2}{k^2 c_s^2 + \Omega^2 - \omega_G^2}, \quad (42b)$$

where ω_G^2 is given by (37).

We shall now determine the steady disk conditions using the vertical averages

$$\Sigma \approx 2\rho h, \quad (43)$$

$$\tau_c \approx \kappa\rho h \approx 1/2\kappa\Sigma, \quad (44)$$

where h is given from hydrostatic equilibrium by

$$h^2 \Omega^2 \approx \bar{R}_g T. \quad (45)$$

Writing $n = \delta_\chi f_G$ from Eqs. (42a) and (42b), the turbulent viscosity is given by

$$\nu_t \approx n/k^2 \approx \chi \frac{3\tau_c^2}{3\tau_c^2 + k^2 h^2} f_G. \quad (46)$$

The factor kh will be taken as a fixed parameter of the model. The flux from the optical surface of the disk F_s , given by the energy equation as

$$F_s = 9/8\Omega^2 \nu_t \Sigma, \quad (47)$$

is related to the accretion rate in a steady disk \dot{M} by

$$F_s = \frac{3}{8\pi} \Omega^2 \dot{M}. \quad (48)$$

In an optically thick medium the flux is

given by the diffusion equation

$$F = \frac{ac}{3} \frac{dT^4}{d\tau}$$

or

$$\int_0^\tau F d\tau = \frac{ac}{3} (T^4 - T_0^4),$$

where T_0 is the temperature at $\tau = 0$. For $\tau \gg 1$, $T^4 \gg T_0^4$, and as a rough average we take

$$\int_0^{\tau_c} F d\tau \approx \frac{1}{2} F_s \tau_c,$$

thus

$$F_s \approx \frac{2acT^4}{3\tau_c}. \quad (49)$$

If we extend the gray atmosphere approximation to the optically thin case (which may be inappropriate if the opacity becomes too line dominated), we find that the flux in a finite slab is given by

$$F \approx acT^4 \tau_c.$$

Taking again the average of F to be $\frac{1}{2}F_s$, we obtain

$$F_s \approx 2acT^4 \tau_c. \quad (50)$$

Following the spirit of Spiegel (1964) and Unno and Spiegel (1966) for perturbations, we join expressions (49) and (50) so that

$$F_s = \frac{2acT^4}{3\tau_c} \frac{3\tau_c^2}{3\tau_c^2 + 1}. \quad (51)$$

We also write, with Eqs. (43)–(45),

$$\chi = \frac{4acT^3}{3\kappa\rho^2c_p} = \frac{8acT^4}{3\tau_c\Sigma\Omega^2} \frac{\bar{R}_g}{c_p}, \quad (52)$$

where we take c_p/\bar{R}_g to be a fixed parameter of the model.

Combining (46), (47), (51), and (52) gives

$$f_G \approx \frac{2c_p t}{9\bar{R}_g}, \quad (53a)$$

where

$$t \equiv \frac{3\tau_c^2 + h^2k^2}{3\tau_c^2 + 1}. \quad (53b)$$

Using $k^2c_s^2 \approx \Gamma_1 k^2 h^2 \Omega^2$, the solution of (52) for vertical gravitational collapse from Eqs. (36) and (42a) is

$$\omega_0^2/\Omega^2 \approx \Gamma_1 k^2 h^2 \frac{1 + f_G}{\gamma + f_G}, \quad (54a)$$

which has a minimal value for the smallest allowed value of kh . For *radial* gravitational collapse from Eqs. (37) and (42b),

$$\omega_0^2/\Omega^2 \approx (1 + 1/kh) \times \left(1 + \Gamma_1 k^2 h^2 \frac{1 + f_G}{\gamma + f_G}\right), \quad (54b)$$

which has a minimal value of about 3.7 for $kh \approx 0.62$ for $\frac{4}{3} < \gamma \leq \frac{5}{3}$. In the optically thick case, $\tau_c^2 \gg (1, k^2 h^2)$, or for $k^2 h^2 \approx 1$, we have $t \approx 1$. In the optically thin cases, $\tau_c^2 \ll (1, k^2 h^2)$, we have $t \approx k^2 h^2$. In both limits we have $\omega_0^2/\Omega^2 \approx \text{constant}$. It is therefore convenient to consider these limiting cases where ω_0^2/Ω^2 is determined solely by the parameters γ , $\Gamma_1 \approx \gamma$, and kh .

Using (43) and (45), we write (36) as

$$\omega_0^2/\Omega^2 \approx \frac{2\pi G\Sigma}{\Omega(\bar{R}_g T)^{1/2}},$$

or

$$\Sigma \approx (\omega_0^2/\Omega^2) \frac{(\bar{R}_g T)^{1/2}}{2\pi G} \Omega, \quad (55)$$

where ω_0^2/Ω^2 is given by either of Eq. (54a) or (54b). We further assume the average opacity has the form

$$\kappa \approx \kappa_0 T^\xi,$$

making Eq. (44)

$$\tau_c \approx \frac{1}{2} \kappa_0 T^\xi \Sigma. \quad (56)$$

Using (55) to eliminate Σ from (56) gives an expression for τ_c in terms of T :

$$\tau_c \approx \left(\frac{\omega_0^2}{\Omega^2}\right) \frac{\kappa_0 \Omega \bar{R}_g^{1/2} T^{\xi+1/2}}{4\pi G}. \quad (57)$$

Further, Eqs. (51) and (48) give another relation between τ_c and T :

$$T^4 \approx \frac{3}{16\pi} \frac{\Omega^2 \dot{M}}{ac} \frac{3\tau_c^2 + 1}{\tau_c}. \quad (58)$$

TABLE II
 $(\eta^{-1} = \frac{1}{2} - \xi, \xi \neq \frac{1}{2})$

$\tau_c \gg 1, (kh)^2$
$T \sim \Omega^{3\eta} \dot{M}^\eta (\omega_0^2/\Omega^2)^\eta$
$h \sim \Omega^{(3/2)\eta-1} \dot{M}^{(1/2)\eta} (\omega_0^2/\Omega^2)^{(1/2)\eta}$
$\Sigma \sim \Omega^{(3/2)\eta+1} \dot{M}^{(1/2)\eta} (\omega_0^2/\Omega^2)^{(1/2)\eta+1}$
$\tau_c \sim \Omega^{12\eta-2} \dot{M}^{(4\eta-1)} (\omega_0^2/\Omega^2)^{4\eta}$
$\alpha_c \sim \Omega^{-(9/2)\eta} \dot{M}^{1-(3/2)\eta} (\omega_0^2/\Omega^2)^{-(1+(3/2)\eta)}$

In the optically thick case with $\tau_c^2 \gg (1, k^2 h^2)$, $\omega_0^2/\Omega^2 \approx \text{constant}$ and

$$T^4 \approx \frac{9}{16\pi} \frac{\Omega^2 \dot{M}}{ac} \tau_c,$$

which gives with Eq. (57)

$$T^{7/2-\xi} \approx \left(\frac{\omega_0^2}{\Omega^2}\right) \frac{9\kappa_0 \bar{R}_g^{1/2}}{64\pi^2 acG} \Omega^3 \dot{M}. \quad (59)$$

From this all other relevant quantities can be calculated. The dependences of T , h , Σ , and τ_c on Ω , \dot{M} , and ω_0^2/Ω^2 are given in Table II. Also given is the dependence of the turbulence coefficient α_c , given by

$$\alpha_c \sim \frac{\dot{M}\Omega}{3\pi\Sigma\bar{R}_g T}. \quad (60)$$

In the optically thin case with $\tau_c^2 \ll (1, k^2 h^2)$, $\omega_0^2/\Omega^2 \approx \text{constant}$ and

$$T^4 \approx \frac{3}{16\pi} \frac{\Omega^2 \dot{M}}{ac} \frac{1}{\tau_c},$$

giving

$$T^{9/2+\xi} \approx \left(\frac{\omega_0^2}{\Omega^2}\right)^{-1} \frac{3}{4} \frac{G\dot{M}\Omega}{ac\kappa_0 \bar{R}_g^{1/2}}. \quad (61)$$

The dependences of T , h , Σ , τ_c , and α_c on Ω , \dot{M} , and ω_0^2/Ω^2 are given in Table III for this case.

The surface density depends on Ω to a power ranging from $\frac{1}{2}$ to $\frac{3}{2}$ for values of ξ from 0 to $\frac{1}{2}$ in the optically thick case, and to a power of slightly greater than 1 in the optically thin case for all $\xi \geq 0$. Thus, when the gravitational instability becomes operative in the outer disk, the surface density decreases rapidly with increasing radius (assuming Keplerian rotation, $\Omega \sim R^{-3/2}$), opposite to the trend of the convective

model. The decline of Σ , coupled to the growth of α_c , with increasing radius is illustrated in Fig. 11, which shows the solution for vertical gravitational collapse (solid lines); the solution from the convective model is indicated in dashed lines. At some radius we expect the convective and gravitational model to join, perhaps smoothly.

While the analysis and results just presented take into account the most important physical effect, namely, the new form of the growth rate, they cannot be considered complete. A complete analysis would have to include changes in the hydrostatic equilibrium equation (i.e., the additional pressure due to self-gravity), non-Keplerian motion, a new expression for energy transport by turbulent motion, and finally the use of the full fifth-order equation for $n(k)$.

The Keplerian motion is altered in the following way: Most of the disk's mass in the convective model resides in the outer radii, and the disk is perhaps truncated at some radius by self-gravity or another mechanism. We therefore imagine the mass distribution of the disk to be toroidal or lobe-like in nature. The self-gravity for this mass distribution depends on the external as well as internal mass at a given radius, unlike for a spherical mass distribution, where the gravity depends only on the internal mass. The innermost region of the disk feels essentially only the pull of the central object. At some intermediate radius the mass in the outer disk is felt, effectively reducing the pull of the central object. If the radial pressure support is negligible such that the radial component of gravitational acceleration is balanced by centrifugal ac-

TABLE III
 $(\eta^{-1} = \frac{1}{2} + \xi)$

$\tau_c \ll 1, (kh)^2$
$T \sim \Omega^\eta \dot{M}^\eta (\omega_0^2/\Omega^2)^{-\eta}$
$h \sim \Omega^{(1/2)\eta-1} \dot{M}^{(1/2)\eta} (\omega_0^2/\Omega^2)^{-(1/2)\eta}$
$\Sigma \sim \Omega^{(1/2)\eta+1} \dot{M}^{(1/2)\eta} (\omega_0^2/\Omega^2)^{1-(1/2)\eta}$
$\tau_c \sim \Omega^{2-4\eta} \dot{M}^{(1-4\eta)} (\omega_0^2/\Omega^2)^{4\eta}$
$\alpha_c \sim \Omega^{-(3/2)\eta} \dot{M}^{1-(3/2)\eta} (\omega_0^2/\Omega^2)^{(3/2)\eta-1}$

celeration, then an effective reduction in gravity causes the rotation rate to decrease and the rotational shear to increase with respect to Keplerian values. At outer radii where most of the mass is concentrated this trend reverses as the attraction of the disk material enhances that of the central object, increasing rotation rates and decreasing rotational shear with respect to Keplerian. At radii far beyond the main concentration of the disk mass the combined mass of the central object and the disk acts as a point source, leading again to Keplerian orbits. The deviation from Keplerian values at the main mass concentration of the disk are expected to be appreciable for a total disk mass comparable to the central mass; the precise properties of the rotational quantities depend sensitively on the exact details of the mass distribution.

A further complication may arise if radial pressure support becomes significant in the self-gravitating part of the disk. This would require a fully two-dimensional treatment.

VII. DISCUSSION

The primordial solar nebula may have been dissipated by turbulence generated by a number of instabilities, e.g., thermal convection, gravitational collapse, infalling material from the outer cloud, etc., with presumably one or more being the predominant mechanism in any given part of the nebula at any given time. In this paper, we have explored the feasibility of constructing a physically consistent and meaningful model of the primordial solar nebula with *turbulence maintained solely by thermal convection*. We have further assumed that the nebular disk is in a stage before (or at the onset of) planetary formation in which gas and dust are mixed homogeneously; indeed, it is the opacity of the dust grains that allows the presence of widespread convection.

Thus far, the traditional method of computing thin accretion disks has been to specify in an ad hoc manner a fixed global parameter α measuring the strength of turbulence generated by all possible unspici-

fied sources. The α method does not shed any light on the physical processes underlying the turbulence, and thus has no ability to predict the structure and behavior of the disk under different physical conditions. In effect, α represents the summed total of our ignorance in accretion disks. This fault is particularly acute in the study of the solar nebula for which direct observational data on protoplanetary disks are still lacking and for which evidence from the present solar system provides only very indirect hints about primordial conditions.

Additional clues may be gleaned from observations of young protostellar objects, e.g., bipolar nebulae, FU Orionis objects, and T Tauri objects, which show some evidence of containing disks, and from protoplanetary systems (Smith and Terrielle, 1984). However, the detailed evolutionary sequence of protostellar objects and their disks, especially with regard to the formation of planets, is still highly speculative.

(a) Comparison of Results with LPB

We find some markedly disparate results from the work of LPB. There are many differences between LPB's treatment and our own (see Sect. VII in Paper I), as well as certain basic similarities, and to ascribe the difference in the final results to one particular cause is probably not valid.

One basic similarity that we have with LPB is that we both use basic convective properties (namely, the superadiabatic temperature gradient and the extent of the convective region) to describe the amount of turbulent viscosity in the disk, and thus the amount of viscous couple between annuli. LPB used a modified mixing length theory that ignores the physical effects of radiative dissipation, rotation, and anisotropy of the convective motions. They further allowed some extraordinary leeway in the definition of the mixing length. Convective turbulence is created and dissipated locally. We in turn use the complete MLT expressions that take radiative dissipation, rotation, and anisotropy into account, and in which we set the characteristic length scale to be the

vertical extent of the convective region. Convective turbulence is created locally, but assumed to be dissipated globally in a smooth manner throughout the convective region.

Another similarity between the models is that they both rely on grain opacities to provide sufficient amounts of opacity for convection to occur under physical conditions thought to be relevant in the primordial disk. LPB used DeCampli–Cameron opacities, which give rise to low-temperature midplane convection from ice-grain opacities and high-temperature midplane convection from iron-grain opacities. Our models use the new opacities by Pollack *et al.* (1986), which feature large moderate-temperature opacities due to silicates and smaller high-temperature opacities due predominantly to iron grains. This gives rise to low-, moderate-, or high-temperature midplane convection, with the high-temperature convection being less efficient than for the DeCampli–Cameron opacities.

Much of the comparison between the results of the two models can be done in terms of the vertically averaged “parameter” describing the efficiency of turbulent convection (α_c). This α -parameter is usually set as a constant of the problem in most disk models. For both LPB and ourselves, α_c is an end product of the model, which we define here as

$$\alpha_c \equiv \langle \nu_t \rangle \frac{\mu\Omega}{R_g T_c}. \quad (62)$$

Since

$$\dot{M} = 3\pi \int_{-\infty}^{\infty} \rho \nu_t dz = 3\pi \Sigma_c \langle \nu_t \rangle, \quad (63)$$

where Σ_c is the surface density contained in the convective regions (and where $\Sigma_c \leq \Sigma$), we obtain

$$\alpha_c = \frac{\dot{M}}{3\pi \Sigma_c} \frac{\mu\Omega}{R_g T_c} \geq \frac{\dot{M}}{3\pi \Sigma} \frac{\mu\Omega}{R_g T_c}. \quad (64)$$

Lin (1981) provides an analytic fit to LPB’s models; noting that his definition of Σ is $\frac{1}{2}$ of ours, one finds $\alpha_c \geq 0.04$ for midplane

convection with ice-grain opacities and $\alpha_c > 0.01$ with iron-grain opacities, independent of radius and \dot{M} . In contrast, our model yields α_c ranging between 10^{-2} and 10^{-4} for each type of midplane convection, depending strongly on both radius and \dot{M} (or, equivalently, effective temperature). Our α_c depends strongly on the superadiabatic temperature gradient, which in turn depends on the opacity. At a given radius, increasing \dot{M} corresponds to increasing the temperature and the opacity, which leads to a larger superadiabatic temperature gradient, which gives a larger α_c . At a given \dot{M} , increasing the radius leads to lower temperatures, and ultimately decreasing values of α_c .

The size of the “mixing length.” In computing the convective turbulence, LPB used the pressure scale height H_p throughout the convective region, which is much smaller than the extent of the midplane convective region far away from the midplane, and which “blows up” at midplane. The larger the mixing length, the larger the convective turbulence viscosity; thus LPB’s turbulent viscosity is strongly peaked at midplane, with little contribution from the outer regions. In fact, LPB’s local value of α ($\approx v_c^2/c_s^2$) at midplane is about 1. The effective length scale in our model is the vertical extent of the convection zone divided by the anisotropy factor, $(1+x)^{1/2} \gg 1$, which is increased by rotational stabilization. The resulting length scale is less than or about H_p near the outer surface of the convection zone.

The expression for turbulent viscosity. LPB used $\alpha \approx v_c^2/c_s^2$ locally, whereas we use an expression that corresponds to $\alpha \approx (\Omega/n)v_c^2/c_s^2$, where $n/\Omega = O(10^{-1})$ on the average.

The different mathematical procedures that each model employs affect both the magnitude and behavior of α_c . The averaging procedure we use on the turbulent viscous dissipation tends to produce lower values of α_c . In Paper I we showed analytically that, with LPB’s equations averaged in a similar manner, $\alpha_c < 10^{-1.5}$; numerical

integrations actually give $\alpha_c \lesssim 10^{-2.5}$. The averaging procedure tends to reduce the strong peaked behavior at midplane of LPB's solutions where their α_c gets its greatest contribution. The insensitivity of LPB's α_c to radius and \dot{M} (i.e., temperature) appears to be in the nature of their local solutions. In LPB's models, the local value of α is always about 1 at midplane and falls sharply with increasing z . They therefore have a very similar function for local α for all thermodynamic conditions, resulting in almost constant values of α_c . In the model presented in this paper, the local value of α with respect to turbulent energy generation is a sensitive function of the convective buoyancy and stabilizing effects of rotation, reflected in the anisotropy parameter.

Another important end product of these models is the size and behavior of the surface density with \dot{M} and radius, which is strongly influenced by the size and behavior of α_c . The larger the turbulent efficiency (α_c), the less material (Σ) is needed to produce a given amount of flux (or \dot{M}). In LPB's model, Σ is roughly constant with R for a given type of midplane convection, and depends on \dot{M} roughly to the $\frac{1}{3}$ power (Lin, 1981). In the model presented in this paper, α_c drops so rapidly with increasing R at fixed \dot{M} that Σ grows with radius. Increasing \dot{M} at fixed R causes α_c to increase so much that Σ decreases. We find the following crude scalings for our model: in low-temperature "ice" models, $\Sigma \sim R\dot{M}^{-1/4}$; in moderate-temperature "silicate" models, $\Sigma \sim R^{5/3}\dot{M}^{-1/2}$; and in high-temperature "iron" models, Σ goes as $R^{5/4}$ and \dot{M} to a power varying between $-\frac{1}{16}$ and $-\frac{1}{2}$.

(b) Comparison with Observational Constraints

There are biases in solar nebula modeling to construct models that are stationary over the radii spanned by the present planets, and to compare the mass distribution of the nebula to the mass of the present planets smeared between their orbits with enough

H and He to give solar abundance (the minimum mass distribution). Neither of these biases is particularly constraining if the nebula evolves dynamically through the epoch of planet formation. A more solid comparison can be made between the general radial temperature distribution in the disk model and the temperature distribution constructed from planetary compositions, provided planetesimal formation was occurring at the particular epoch this solar nebula model might represent (Fig. 10).

Neither LPB's nor our mass distribution compares favorably with the minimum mass distribution, which has $\Sigma \sim R^{-3/2}$, at least in the outer orbits (Weidenschilling, 1977).

For a stationary convective disk for radii at least as small as Mercury's, one requires that grains be condensed there to provide the necessary opacity. This limits the temperature and \dot{M} . At the same time, one wishes to have a decent fit between midplane temperatures and estimated compositional temperatures (Lewis, 1974) versus radius. Lin (1981) finds a best fit of $\dot{M} \approx 10^{19}$ g sec⁻¹. We find a best fit (Fig. 10) for $\dot{M} = 10^{18}$ to $10^{18.5}$ g sec⁻¹, being somewhat lower as a consequence of our lower turbulent efficiency. The mass of LPB's disk is about $0.01M_\odot$, for which the disk's self-gravity is negligible. Our disk is unstable to gravitational instability at a radius between the orbits of Saturn and Uranus; this implies a massive disk with $M_d > 0.1M_\odot$. The time for the disk to dissipate at a given accretion rate, $\tau_d = M_d/\dot{M}$, is about $\sim 10^5$ years for LPB's model and $> 2 \times 10^6$ years for the model presented here.

The time scale associated with the infall of the molecular cloud in the protostellar (notably T Tauri) stage is $\sim 10^6$ years. Observations suggest the first 10^5 years are spent in a dynamic stage of bipolar outflow (Lada, 1985). It is possible that the bipolar outflow is powered by release of gravitational potential energy in an accretion disk close to the central condensation. If so, then one infers that the (dynamic) disk is dispersed in $\sim 10^5$ years and suggests that

high- \dot{M} , high- α models pertain to this stage. Adams *et al.* (1987) suggest that T Tauri stars, after the bipolar outflow stage, settle into a stage with quiescent disks with virtually no intrinsic luminosity; radiation from the disks is from reprocessing of protostellar photons. Hartmann and Kenyon (1985) suggest that FU Orionis-like outbursts arise in T Tauri stars after a very-low- α ($\sim 10^{-4}$) disk or torus accumulates enough matter for high temperatures to develop and grains to evaporate, drastically lowering the opacity; at this point a "cataclysmic" outburst is suggested to occur in the disk, in analogy with the outburst mechanisms suspected to operate in dwarf novae (Faulkner *et al.*, 1983; Cannizzo and Wheeler, 1984). If outbursts in FU Orionis stars are disk phenomena, then again a high- \dot{M} , high- α accretion occurs onto the central star. Our models suggest that convection is too weak to generate turbulent transport corresponding to the energetic, high- α stages of protostellar systems, and that another mechanism must be involved. While it may be tempting to apply our convective model to the more quiescent, low- α stages of the disk, irradiation of the disk's surface by the young star and possible heating of the disk's surfaces by residual infall of matter may suppress this by causing the vertical temperature gradient to be subadiabatic for low enough accretion rates.

It is not clear in previous scenarios of protostellar evolution at which point planetesimal or planetary formation is initiated. Clearly, at some point the grains separate from the gas to commence the formation of planetesimals. Weidenschilling (1984) has shown that while turbulence initially promotes coagulation of grains to small sizes, larger coagulations are destroyed by collisions using LPB's convective model. It is possible that with the lower convective speeds predicted by our model ($v_c \leq 0.01c_s$) the grains could coagulate to larger sizes. However, Weidenschilling also points out that when grains coalesce in the dust-gas mix that the opacity drops, eventually shut-

ting down the convective turbulence. Therefore an understanding of this crucial stage in planetary formation can only be achieved by detailed models that follow the dynamical behavior of the opacity in the disk as a function of grain size distribution as well as temperature. The credibility of all convective solar nebula models to date has suffered from this neglect.

(c) *Implications of the Disk Instabilities*

Our model predicts that, at an epoch when dust and grains were homogeneously mixed, the solar nebula was massive enough for gravitational instabilities to occur. *If*, as suggested by Goldreich and Lynden-Bell (1965) and Paczyński (1978), motions generated by gravitational collapse can in some way be transformed into turbulent motion (e.g., by interaction with rotational shear), the collapse of the disk could be balanced in a marginal state by heating from turbulent energy generation. We have investigated these models in Section VI. We find that the surface density falls rapidly with increasing radius, which could suggest a natural mechanism for truncating the inner primordial nebula from the outer cloud.

On the other hand, *if* gravitational collapse *cannot* be converted into turbulent motion, then the scenario for a steady state convective disk breaks down at radii roughly comparable to Uranus's orbit, beyond which an unsteady region might have existed where gravitational instabilities developed unchecked, provided enough material could accumulate there initially. The "gravitational instability" (GI) is unattractive to proponents of the "core instability" (CI) hypothesis for formation of the giant planets. This is so because the GI scenario suggests that giant planets formed from instabilities in which gas (H and He) and high-Z material were homogeneously mixed. A basic tenet of the CI hypothesis, however, is that the outer planets developed from solid, high-Z objects that, at a critical mass, initiated rapid contractions of

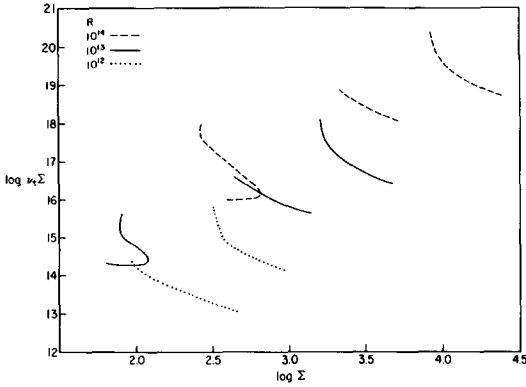


FIG. 12. The mass transfer term $\nu_i \Sigma$ (in g sec^{-1}) as a function of Σ (in g cm^{-2}) for $\log R = 12, 13,$ and 14 . As Σ increases, the curves correspond to the ice, silicate, and iron models; for $\log R = 12$, only the silicate and iron models are plotted.

their gaseous envelopes; this hypothesis appears to fit models of the present planets far better than the GI model (Pollack, 1984).

A major problem lies in the inverse dependence of the accretion rate (i.e., the viscous couple) on the surface density Σ (see Sect. V; Fig. 12). As discussed in Pringle (1981), such a dependence may lead to the instability discovered by Lightman and Eardley (1974). For a short-wavelength sinusoidal perturbation, the growth rate n of the instability is

$$n \approx \frac{3}{4} \langle \nu_i \rangle k_R^2 \left(- \frac{\partial \ln \dot{M}}{\partial \ln \Sigma} \right), \quad (65)$$

where k_R is a radial wavenumber. In our solution, we typically find $-\partial \ln \dot{M} / \partial \ln \Sigma \gtrsim 2$; thus, $n \gtrsim \frac{3}{2} k_R^2 \langle \nu_i \rangle \approx \frac{3}{2} (k_R h)^2 \alpha_c \Omega$. The rates for establishing vertical hydrostatic and thermal equilibria are Ω and $\alpha_c \Omega$, respectively, where a typical value of $\alpha_c = 10^{-3}$ is found in our convective models. For intermediate wavenumbers, $k_R h \sim 1$, the rate of growth for this instability exceeds that for maintaining vertical thermal equilibrium, and for large enough wavenumbers exceeds even the rate for maintaining vertical hydrostatic equilibrium.

Our “steady disk” would therefore tend

to form rings, or perhaps clumps for non-axisymmetric perturbations, quite rapidly. The evolution of this instability is not straightforward, since radial gradients and time-dependent terms would become significant in the process. It is possible, for instance, that as the instability develops, a self-regulating mechanism acts to inhibit disruption of the disk, at least on some scales. It is clear, in any case, that the solar nebula cannot evolve into precisely the type of “steady” disk structure predicted by our convective model. Without proper treatment of radial and time derivatives, we cannot speculate the extent to which the steady disk structure, if such exists, deviates from this convective model.

LPB’s convective model is stable against this diffusive instability with $\partial \ln \dot{M} / \partial \ln \Sigma \approx 3$. Other formulations of the turbulent energy generation and dissipation by convective motions could conceivably yield intermediate results with both stable and unstable regimes of parameter space. A convective nebula might then be subject to a hysteresis effect like that thought to occur in dwarf novae (cf. Bath and Pringle, 1985). The problem of the radial stability of steady accretion flows with convective turbulence certainly requires further examination. We need to clarify the manner in the distribution of generation and dissipation of convective turbulence affects the stability of the solutions. We hope that large-scale numerical simulations of turbulent flows in a disk geometry will aid us in determining the validity of these prescriptions of convective turbulence. More detailed numerical models are also needed to follow the development of the instability should it occur.

VIII. CONCLUSIONS

In this paper we have presented results from a new convective model of the primordial solar nebula. This model incorporates new grain opacities by Pollack *et al.* (1986) and the prescriptions to treat convective turbulence suggested by Canuto and Gold-

man (1985) and Canuto *et al.* (1984), which allow us to include directly the effects of radiative energy losses, rotation, and anisotropy of convective motions. The turbulence is generated in the convective vertical structure straddling the midplane in proportion to the local convective buoyancy, which peaks well away from midplane. The turbulent energy deposition is assumed to be distributed smoothly throughout the convective midplane region.

The results are, in brief:

(1) We find lower, more variable values of the turbulent viscosity parameter α (typically from 10^{-2} to 10^{-4}) than in earlier models by Lin, Papaloizou, and Bodenheimer (α from $10^{-1.5}$ to 10^{-2}). Our α appears to be highly sensitive to the local opacity.

(2) We find an accretion rate \dot{M} of about $10^{18.5}$ g sec $^{-1}$ ($5 \times 10^{-8} M_{\odot}$ year $^{-1}$) for a steady (constant \dot{M}) structure having a $1 M_{\odot}$ central object, extending in as far as Mercury's present orbit, and having temperatures corresponding to estimated compositional temperatures of the present planets (Fig. 10). However, for a lower mass central object, the maximal value of \dot{M} by this constraint increases as $M^{-3/4}$ to M^{-3} , depending on the sequence of events in inner planet formation.

(3) The surface density Σ increases steadily with radius in steady models, leading to satisfaction of Jean's criterion for gravitational collapse at a radius comparable to that of Uranus, and giving a disk mass greater than $0.1 M_{\odot}$.

(4) We find a long time scale for dispersal of the disk of greater than 2×10^6 years, compared with suspected time scales of 10^5 – 10^6 years in young stellar objects.

(5) Perhaps the most important result we find is an inverse \dot{M} – Σ relation in most of the parameter space, implying a Lightman–Eardley-like diffusive instability operating radially.

The occurrence of the Jean's instability at outer orbits and the Lightman–Eardley instability throughout the disk strongly suggests that the inner solar nebular could not

have developed from the collapsing molecular cloud in the form of the "steady" disk models portrayed herein if convection were the sole source of turbulence. The long time scale for dispersal of the disk also argues that another more efficient source of turbulence was required to dissipate the gaseous disk.

There are a number of improvements that we urge and anticipate in the physics of future modeling of primitive solar and stellar nebulae:

(1) Rather than the snapshot approach used in all computations thus far, where one models an imagined epoch of the nebula with a steady disk of perfectly coupled dust and gas, one should perform more realistic modeling of formation of the inner protoplanetary disk from infalling material from the outer cloud; and, inclusive of this,

(2) realistically model the dynamic behavior of the dust opacity and grain size distribution in the disk.

The sensitivity of the occurrence of the of the inverse \dot{M} – Σ relation (and the concomitant radial diffusive instability) to the vertical distribution of turbulent energy generation and dissipation deserves further study and begs for better basic models of turbulent transport in this kind of geometry and rotational shear. Efficient numerical simulations on supercomputers, now possible in principle, may soon provide answers to this problem.

Further observations of protostellar objects and protoplanetary systems should provide tighter constraints on conditions in and evolution of primordial stellar nebulae.

ACKNOWLEDGMENTS

We are grateful to Al Cameron, John Cannizzo, Pat Cassen, Doug Lin, Steve Ruden, Frank Shu, David Stevenson, Mike Torbett, and Stu Weidenschilling for useful and enlightening discussions and comments. Part of this work was done while one of the authors (W.C.) held a NRC–NASA Research Associateship. Doris Smith skillfully typed the manuscript.

REFERENCES

- ADAMS, F. C., C. J. LADA, AND F. H. SHU (1987). Spectral Evolution of Young Stellar Objects. *Astrophys. J.* **312**, in press.

- ALLEN, C. W. (1973). *Astrophysical Quantities*, pp. 30, 48. Oxford Univ. Press (Athlone), London/New York.
- BATH, G. T., AND J. E. PRINGLE (1985). Cataclysmic variables: Theoretical overview. In *Interacting Binary Stars* (J. E. Pringle and R. A. Wade, Eds.), pp. 177–195. Cambridge Univ. Press, London/New York.
- CABOT, W., V. M. CANUTO, O. HUBICKYJ, AND J. B. POLLACK (1987). The role of turbulent convection in the primitive solar nebula: I. Theory. *Icarus* **69**, 387–422.
- CAMERON, A. G. W. (1973). Abundance of the elements in the Solar System. *Space Sci. Rev.* **15**, 121–146.
- CAMERON, A. G. W., AND M. R. PINE (1973). Numerical models of the primitive solar nebula. *Icarus* **18**, 377–406.
- CANNIZZO, J. K., AND J. C. WHEELER (1984). The vertical structure and stability of alpha model accretion disks. *Astrophys. J. Suppl.* **55**, 367–388.
- CANUTO, V. M., AND I. GOLDMAN (1985). Analytical model for large scale turbulence. *Phys. Rev. Lett.* **54**, 430–433.
- CANUTO, V. M., I. GOLDMAN, AND O. HUBICKYJ (1984). A formula for the Shakura–Sunyaev turbulent viscosity parameter. *Astrophys. J.* **280**, L55–L58.
- CLAYTON, D. D. (1968). *Principles of Stellar Evolution and Nucleosynthesis*. McGraw–Hill, New York.
- COX, J. P., AND R. T. GIULI (1968). *Principles of Stellar Structure*, Chap. 14. Gordon & Breach, New York.
- DECAMPLI, W. M., AND A. G. W. CAMERON (1979). Structure and evolution of isolated giant gaseous protoplanets. *Icarus* **38**, 367–391.
- DECAMPLI, W. M., A. G. W. CAMERON, P. BODENHEIMER, AND D. C. BLACK (1978). *Ortho* and *para* hydrogen in dense clouds, protoplanets and planetary atmospheres. *Astrophys. J.* **223**, 854–858.
- FAULKNER, J., D. N. C. LIN, AND J. PAPALOIZOU (1983). On the evolution of accretion disc flow in cataclysmic variables. I. The prospect of a limit cycle in dwarf nova systems. *Mon. Not. R. Astron. Soc.* **205**, 359–375.
- GOLDREICH, P., AND D. LYNDEN-BELL (1965). Gravitational instability of uniformly rotating disks. *Mon. Not. R. Astron. Soc.* **130**, 97–124.
- HARTMANN, L., AND S. J. KENYON (1985). On the nature of FU Orionis objects. *Astrophys. J.* **299**, 462–478.
- HERZBERG, G. (1950). *Spectra of Diatomic Molecules*, pp. 466–532. Witton, New York.
- KELLMAN, S. A., AND J. E. GAUSTAD (1969). Rosseland and Planck mean absorption coefficients for particles of ice, graphite and silicon dioxide. *Astrophys. J.* **157**, 1465–1467.
- KNACKE, R. F. (1968). Extinction by interstellar silica grains. *Nature* **217**, 44–45.
- LADA, C. J. (1985). Cold outflows, energetic winds, and enigmatic jets around young stellar objects. *Annu. Rev. Astron. Astrophys.* **23**, 267–317.
- LEWIS, J. S. (1974). The temperature gradient in the Solar System. *Science* **186**, 440–443.
- LIGHTMAN, A. P., AND D. M. EARDLEY (1974). Black holes in binary systems: Instability of disk accretion. *Astrophys. J.* **187**, L1–L3.
- LIN, D. N. C. (1981). Convective accretion disk model for the primordial solar nebula. *Astrophys. J.* **246**, 972–984.
- LIN, D. N. C., AND P. BODENHEIMER (1982). On the evolution of convective accretion disk models of the primordial solar nebula. *Astrophys. J.* **262**, 768–779.
- LIN, D. N. C., AND J. PAPALOIZOU (1980). On the structure and evolution of the primordial solar nebula. *Mon. Not. R. Astron. Soc.* **191**, 37–48.
- MATHIS, J. S., W. RUMPLI, AND K. H. NORDSICK (1977). The size distribution of interstellar grains. *Astrophys. J.* **217**, 425–433.
- MOROZOV, A. G., YU. M. TORGASHIN, AND A. M. FRIEDMAN (1985). Turbulent viscosity in a gravitating gaseous disk. *Sov. Astron. Lett.* **11**(2), 94–97.
- OSTERBROCK, D. E. (1962). On *para* and *ortho* hydrogen molecules in interstellar space. *Astrophys. J.* **136**, 359–362.
- PACZYNSKI, B. (1978). A model of self-gravitating disk. *Acta Astron.* **28**, 91–109.
- POLLACK, J. B. (1984). Origin and history of the outer planets. *Annu. Rev. Astron. Astrophys.* **22**, 389–424.
- POLLACK, J. B., C. P. MCKAY, AND B. M. CHRISTOFFERSON (1986). A calculation of the Rosseland mean opacity of dust grains in primordial Solar System nebulae. *Icarus* **64**, 471–492.
- PRINGLE, J. E. (1981). Accretion disks in astrophysics. *Annu. Rev. Astron. Astrophys.* **19**, 137–162.
- SAFRONOV, V. S. (1969). *Evolution of the Protoplanetary Cloud and Formation of the Earth and Planets*. NASA TT F-677, 1972.
- SAFRONOV, V. S. (1980). Some problems of evolution of the solar nebula and of the protoplanetary cloud. In *E. Fermi Int. School*, Vol. 73, pp. 73–81.
- SMITH, B. A., AND R. J. TERRILE (1984). A circumstellar disk around Beta Pictoris. *Science* **226**, 1421–1424.
- SPIEGEL, E. A. (1964). The effect of radiative transfer on convective growth rates. *Astrophys. J.* **139**, 959–974.
- UNNO, W., AND E. A. SPIEGEL (1966). The Eddington approximation in the radiative heat equation. *Proc. Astron. Soc. Japan* **18**, 85–95.
- WEIDENSCHILLING, S. J. (1977). The distribution of mass in the planetary system and solar nebula. *Astrophys. Space Sci.* **51**, 153–158.
- WEIDENSCHILLING, S. J. (1984). Evolution of grains in a turbulent solar nebula. *Icarus* **60**, 553–577.